2009

A study of the self-assembly of water-soluble porphyrins in aqueous solution

Javoris Hollingsworth

Louisiana State University and Agricultural and Mechanical College

A STUDY OF THE SELF-ASSEMBLY OF WATER-SOLUBLE PORPHYRINS IN AQUEOUS SOLUTION

A Thesis

Submitted to the Graduate Faculty of the
Louisiana State University and
Agricultural and Mechanical College
in partial fulfillment of the
requirements for the degree of
Master of Science

in

The Department of Chemistry

by
Javoris Hollingsworth
B.S., Georgia Southern University, 2007
August 2009

To my family and teachers who supported my growth along this ongoing educational journey

TABLE OF CONTENTS

LIST OF ABBREVIATIONS AND SYMBOLS

AUC = Analytical Ultracentrifugation

DLS = Dynamic Light Scattering

DCM = Dichloromethane (CH_2Cl_2)

EM = Electron Microscopy

H$_2$TPPP = *Meso*-Tetrakis(4-Phosphonatophenyl) Porphyrin

H$_2$TPPS = *Meso*-Tetrakis(4-Sulfonatophenyl) Porphyrin

MS = Mass spectroscopy

m/z = Mass to charge ratio

NMR = Nuclear Magnetic Resonance

PDT = Photodynamic Therapy

SAXS = Small Angle X-ray Scattering

SEC = Size Exclusion Chromatography

SE = Sedimentation Equilibrium

SV = Sedimentation Velocity
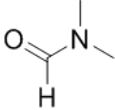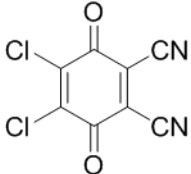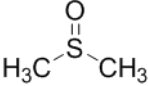
TFA = Trifluoroacetic acid

TLC = Thin Layer Chromatography

TMS = Tetramethylsilane

TPP = 5, 10, 15, 20-tetraphenylporphyrin

ABBREVIATIONS WITH SELECTED STRUCTURES

DMF	**Dimethylformamide**
DDQ	**2,3-dichloro-5-6-dicyanobenzoquinone**
DMSO	**Dimethylsulfoxide**

ABSTRACT

In nature, self-assembly processes of biologically active organic molecules often occur, resulting in formation of dimers and higher oligomers of various and sometimes complex structures. This natural occurrence of self-organization has been the subject of research, with the aim of understanding and possibly modulating the aggregation behavior of biological molecules. The *meso*-tetrakis(4-phosphonatophenyl) porphyrin, H_2TPPP was synthesized, purified, and characterized. Its self-assembly was studied in aqueous solutions as a function of pH and time. The variations on the λ_{max} and shape of the Soret band of this porphyrin in the absorption spectra when altering the pH indicated the pH dependency in the hierarchical self-assembly of H_2TPPP in aqueous solution. The aggregation as a function of time was monitored via fluorescence spectroscopy, where the emission intensity decrease suggests self-quenching and aggregation. Small angle x-ray scattering experiments were conducted in an attempt to obtain structural information for the self-organized porphyrin complexes. Analytical ultracentrifugation techniques confirmed reported SAXS results and also revealed the self-associative behavior of the aggregates.

CHAPTER 1 INTRODUCTION: SYNTHESIS AND STUDY OF PORPHYRIN AGGREGATION BEHAVIOR

In nature, self-assembly processes of biologically active organic molecules often occur, resulting in formation of dimers and higher oligomers of various and sometimes complex structures. This natural occurrence of self-organization has been the subject of research, with the aim of understanding and possibly modulating the aggregation behavior of biological molecules. For instance, one of the most prominent epidemics present today is Alzheimer's disease. It is known as a primary cause of dementia, which is a decline or loss in memory and other cognitive abilities. According to the Alzheimer's Association, more than 5 million Americans are living with this fatal illness. Scientists have associated the cause of this disease to the aggregation of plaque or tangles in the brain.[1] Accumulation of these aggregates is due to hierarchical self-aggregation of abnormal proteins, which currently has no known method of control. The work discussed in this thesis applies several analytical techniques to explore a similar self-assembly process of water-soluble porphyrins in aqueous solution.

Chapter 1 provides an overview of porphyrins and details about their properties, methods of synthesis, and aggregate types via UV-Vis and florescence spectroscopy. Chapter 2 expounds on analytical ultracentrifugation and the sedimentation equilibrium experiments used to determine the self-associative behavior and size of the porphyrin aggregates. Chapter 3 contains information on the subject of small angle x-ray scattering and its application for discovering the morphology of the self-assembled porphyrins in solution.

1.1 Porphyrin Self-Assembly

Hierarchical self-assembly is a time-dependent process that exploits intermolecular interactions by which specific structures are formed sequentially from the assembly of simpler constituents.[2] This method of synthesis is not thoroughly understood and is still being

investigated. Recent studies[3] suggest that the assembly process is based on the "Sergeant-Soldier" Principle (Figure 1.1). According to the principle, pre-determined conditions dictate the initial complex formation (sergeant) and the proceeding assembly of the monomeric units (soldiers) follow the same architectural formation as the sergeant. For this investigation, our "simple" elements of interest are water-soluble porphyrins. Porphyrins are versatile building blocks because of their ability to self-assemble spontaneously into aggregates through non-covalent interactions, depending on their electronic and steric properties.[4]
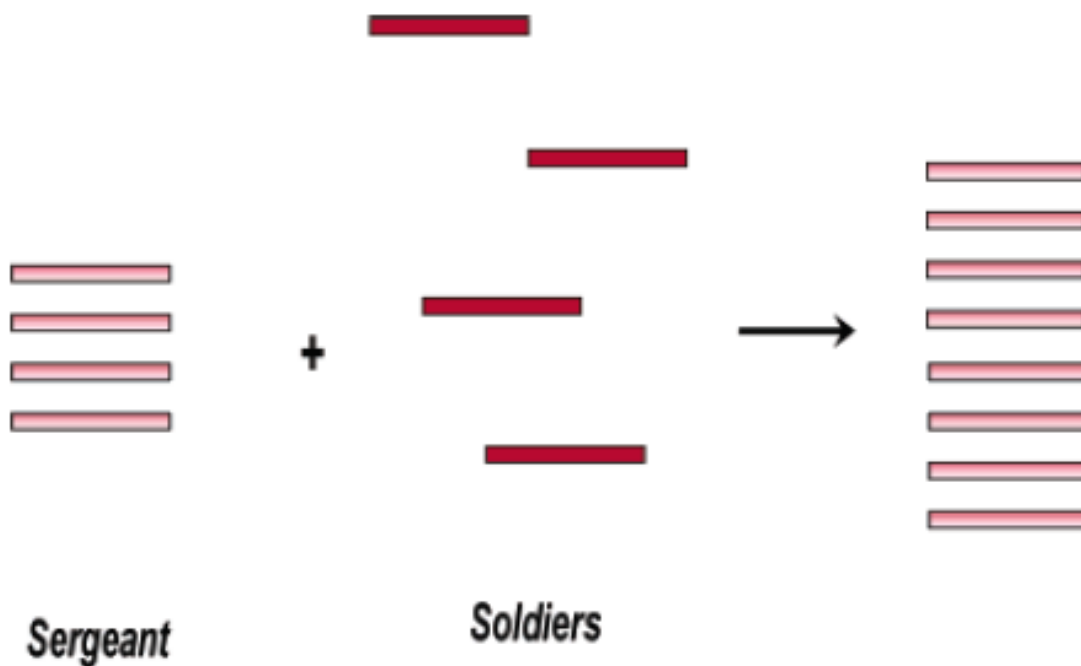
Figure 1.1 An illustration of homo-self-aggregation via sergeant–soldier principle. The monomer units (Soldiers) follow and continue the formation of the initial complex (Sergeant).[3]

1.2 Structure of Porphyrins

Porphyrins are tetrapyrrole macrocycles that possess 22 π electrons; 18 are incorporated in any one delocalization pathway[5] (Figure 1.2). Based on Hückel's rule, porphyrins are highly aromatic. These aromatic properties contribute to many useful applications, particularly in the field of medicine. For instance, products such as Photofrin II® utilize the photochemical capabilities of porphyrins in photodynamic therapy (PDT) for the treatment of malignant tumors.[6] The binary cancer treatment, PDT, incorporates a photosensitizer that is excited to the singlet state as a result of absorbing a specific wavelength of light. Consequently, cytotoxic Reactive Oxygen Species (ROS) are generated and this kills tumor cells.[7-9]
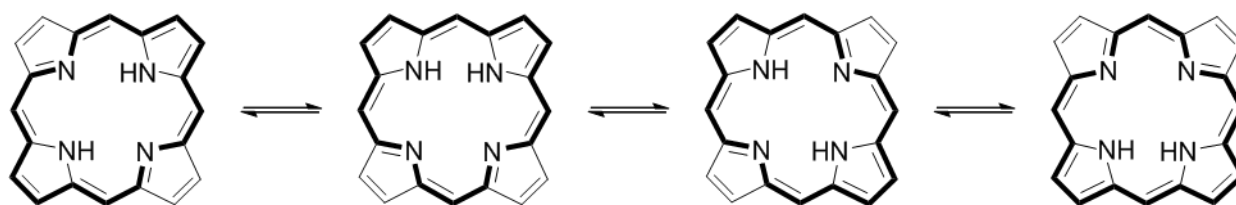
Figure 1.2 Structure of a fundamental porphyrin with 18 π delocalized pathway.

Excited state properties of porphyrins are the basis of their unique photochemistry. The prominent electronic transition for porphyrins is $\pi \rightarrow \pi^*$ transitions which are associated with the porphyrin ring.[5] As a result of protonation and self-aggregation, the compounds adopt new photochemical characteristics that are different from the monomeric properties. Thus, spectroscopic techniques can be employed to monitor the aggregation process by examining the changes in the photophysical properties over time.

The self-assembly phenomena of porphyrins have been explored for homo- and hetero-self-aggregates, but there is limited knowledge of this process in aqueous solution.[10, 11] Studies were performed to test the pH dependency of hierarchical homo-self-assembly of *meso-*

tetrakis(4-phosphonatophenyl)porphyrin, H_2TPPP (Figure 1.3a). The aggregation behavior of H_2TPPP was examined in aqueous solution courtesy of the polar properties of the compound. The phosphonic groups, which are dibasic, can form both acid and neutral salts. The PO_3H^- is electron-withdrawing and the PO_3^{-2} group is electron-donating.[12] These electronic properties dictate the pK_a values of the constituents, which further determines the hydrogen bonding of the monomeric species at each protonation equilibrium step.
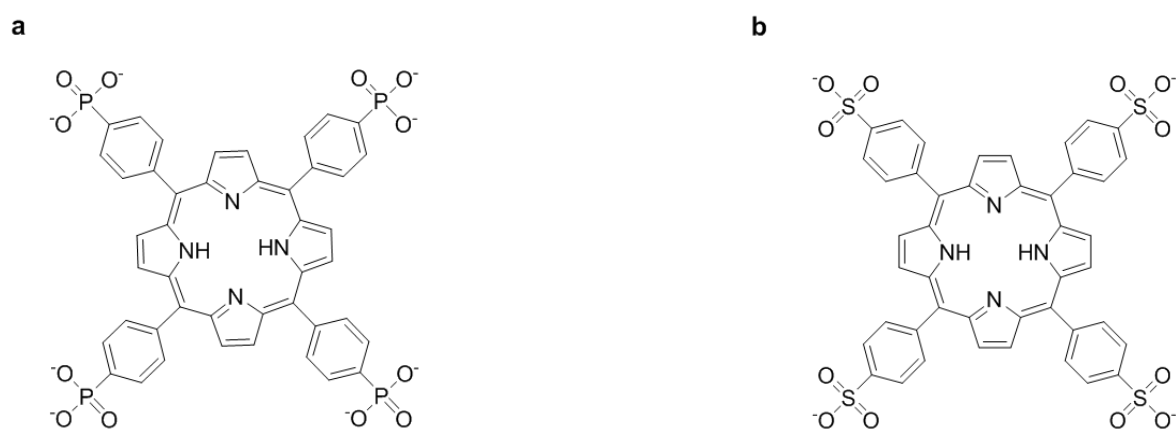
Figure 1.3 Structures of (a) H_2TPPP and (b) H_2TPPS .

  Porphyrins are considered amphoteric due to the inner pyrrolic nitrogens possessing acidic and basic properties.[13] The polyprotic character of H_2TPPP is one of the driving forces that dictate specific time-dependent kinetic aggregation routes taken by the normal thermodynamic species. Three possible steps for protonation can be achieved with this particular porphyrin and each step, in theory, yields a different aggregate. The thermodynamic pathway is determined by hydrogen bonding at particular protonation sites while at protonation equilibrium (Figure 1.4). In H_2TPPP, the phosphonate groups ($pK_a \approx 7.8$) are protonated first. The nitrogen atoms ($pK_a \approx 5.4$) within the macrocycle core are protonated in the second step. The last step is the second protonation of the phosphonate groups ($pK_a \approx 2.4$). In contrast, *meso*-tetrakis(4-

sulfonatophenyl) porphyrin, H_2TPPS, (Figure 1.3b) does not possess multiple pathways of aggregation because it is an anionic porphyrin (Figure 1.4b). The macrocycle core nitrogen atoms ($pK_a \approx 4.8$) is positively charged following protonation and interacts with the negative charges on the sulfonate groups, which leads directly to one thermodynamic product.[3] Hence, unlike the polyprotic H_2TPPP, the anionic H_2TPPS species should not be capable of exhibiting any hierarchical self-assembly behavior. In order to recognize distinct behavioral and structural differences involved in hierarchically driven processes, the aggregation of H_2TPPP and H_2TPPS were compared. The hydrogen bonding during protonation steps is a relatively much quicker process than the aggregation of the monomeric porphyrins, which increases the feasibility of observing the variations within the two pathways.[14]
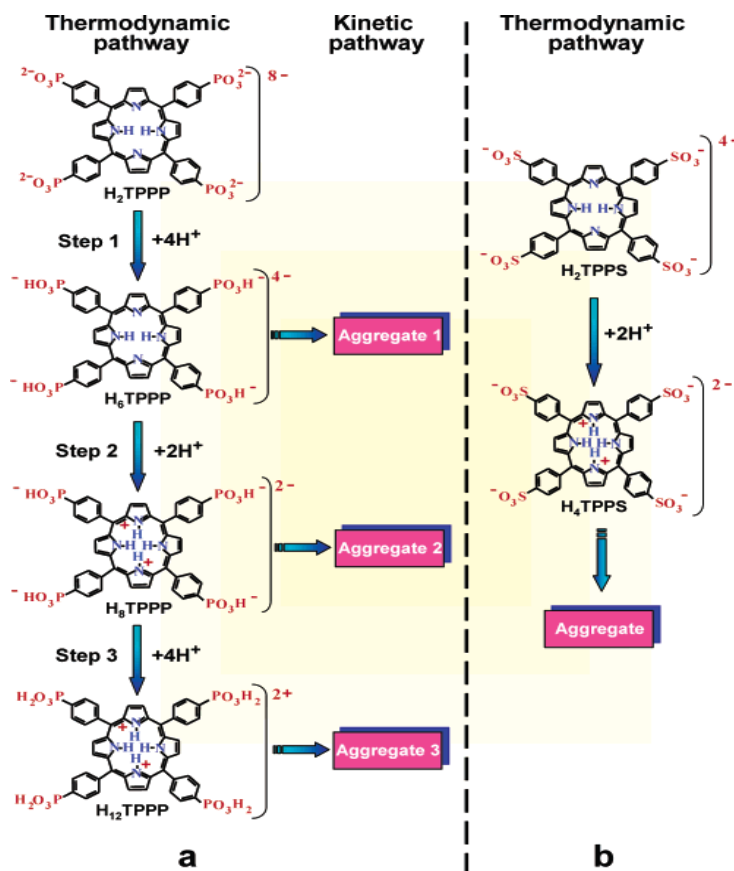
Figure 1.4 Potential aggregation pathways of (a) H_2TPPP and (b) H_2TPPS after protonation.[14]

1.3 Porphyrin Aggregate Characterization

Porphyrins are capable of forming two main types of aggregates in solution, dubbed J-type and H-type. H-aggregates are parallel monomeric units stacked *face-to-face*, whereas J-aggregates are *edge-by-edge*.[15] Several one-dimensional assembly patterns exist for J-aggregates in solution, such as ladder, staircase, and brickstone type arrangements (Figure 1.5). These arrangements are formed based on specific electrostatic interactions between the charged regions of neighboring species. The terms J- and H-aggregate were coined from their spectral shifts. Bathochromically shifted J-bands (J for Jelly, one of the first investigators of these shifts) and hypsochromically shifted H-bands (H for hypsochromic) are observed for J- and H-aggregates, respectively. For bathochromic shifts, spectral bands migrate to a lower frequency (longer wavelength) and are informally referred to as red shifts. In contrast, hypsochromic shift refers to the migration of a spectral band to a higher frequency (shorter wavelength) and is commonly known as a blue shift.[16] These spectral shifts are typically a result of a change in a molecular entity or a change in environment.

a) H-aggregate   b) ladder   c) staircase   d) brickstone
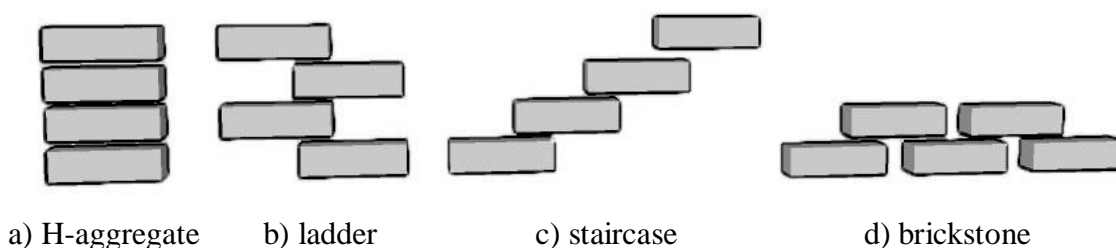
Figure 1.5 Representation of potential assembly patterns for (a) H-aggregates and (b-d) J-aggregates. Each block represents a protonated porphyrin species.

The dynamics of the absorption band shifts exhibited by the specific aggregates is based on the excitonic splitting theory. H- and J-aggregates possess monomer transition dipoles which are aligned parallel or perpendicular, respectively, to the neighboring molecules. The parallel orientation of monomers in H-aggregates leads to a transition to the upper excited state (blue

shift). In contrast, "head-to-tail" arranged monomers in J-aggregates cause a transition to a lower excited state (red shift) (Figure 1.6).[16] When chromophores are aligned in a parallel fashion, two new excitonic bands are generated; a lower and higher energy state. The lower energy state is more stable for H-aggregates, which explains the fast transition from the excited state to the ground state. As a consequence, the quantum yield is low and there is a large Stokes shift. In terms of J-aggregates, only transitions to low energy states are allowed. Due to the transition limitation, J-aggregates have a high quantum yield and small Stokes shift. The π orbitals of the neighboring molecules are closely associated and leads to strong exciton coupling; resulting in the J-aggregate absorption being exchange narrowed.[17]
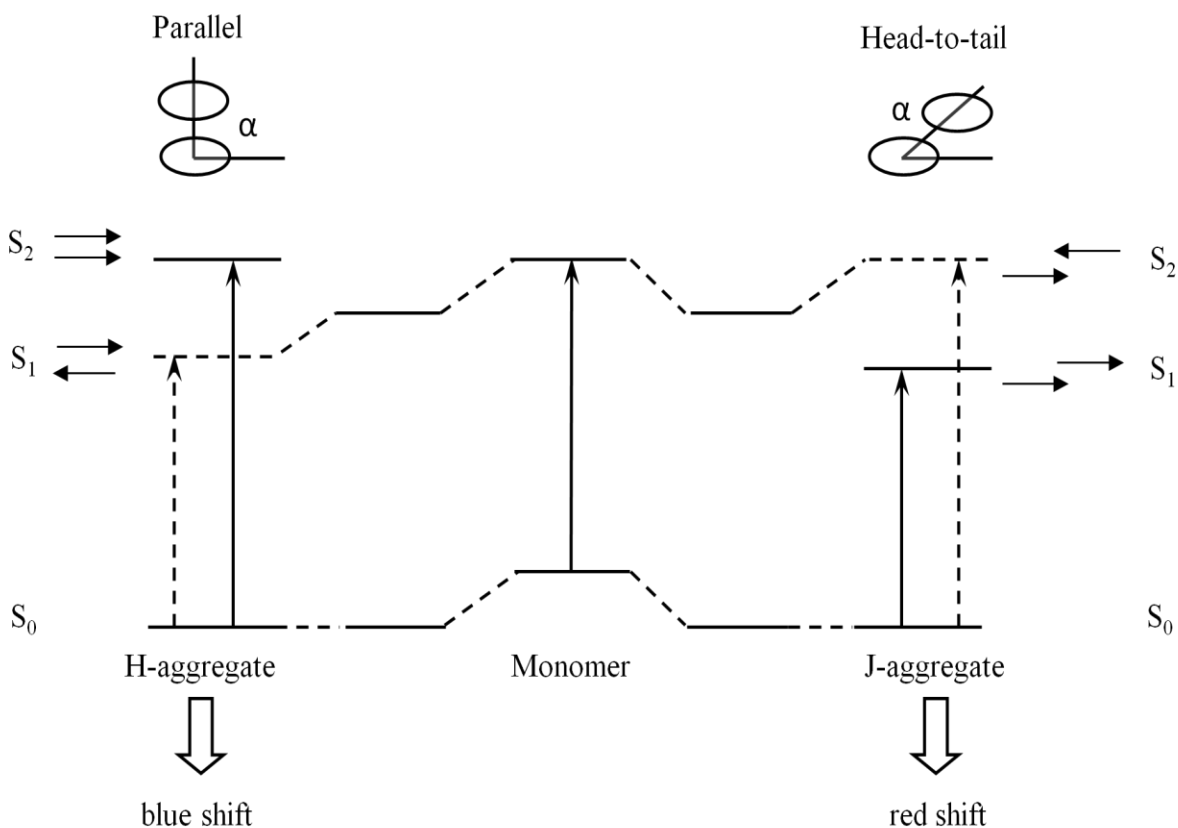
Figure 1.6 Simplified Jablonski diagram of the chromophore arrangement in J- and H-aggregates that lead to spectral shifts based on molecular exciton theory.[16]

1.4 Results and Discussion

1.4.1 Synthesis of *Meso*-tetrakis(phosphonatophenyl) Porphyrin

In 1936, tetraphenylporphyrin was first synthesized by Paul Rothemund.[18] The Rothemund method required harsh reaction conditions; pyrrole **(1.1)** and benzaldehyde **(1.2)** in pyridine at 150 °C for approximately 24 hours.[19] Consequently, the desired tetraphenylporphyrin (TPP) **(1.3)** was obtained in low yields (Scheme 1.1).
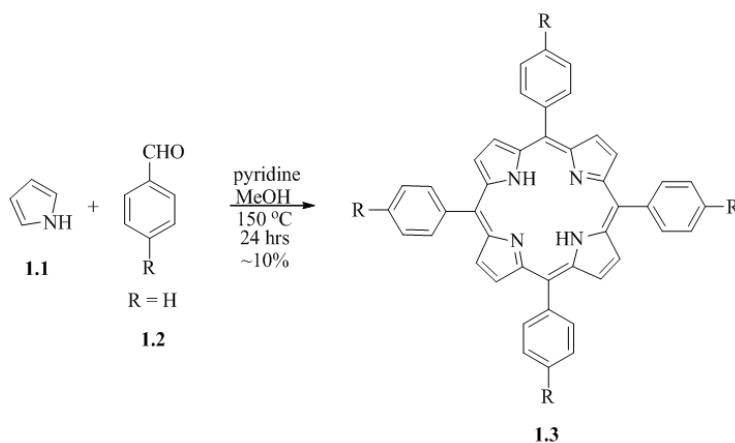
Scheme 1.1 Synthesis of TPP via Rothemund method.[19]

The Rothemund method was later modified by Adler and Longo under relatively milder reaction conditions. A wider range of substituents became feasible as a result of the conditions being less harsh. This new method of synthesizing TPP was also simpler than the original method. Reaction rates were faster and the resulting yields were higher (20 ± 3 %).[20] (Scheme 1.2) The reaction modifications included refluxing pyrrole **(1.1)** and benzaldehyde **(1.2)** in propionic acid for 30 minutes at 141 °C. Although the Adler–Longo method provides a higher yield of TPP under comparatively mild reaction conditions, there are still some associated problems. For instance, a high degree of tar is produced during the reaction which makes purification very difficult.[18] Regardless of this drawback, the Adler-Longo method is still one of the most efficient in the synthesis of TPP.
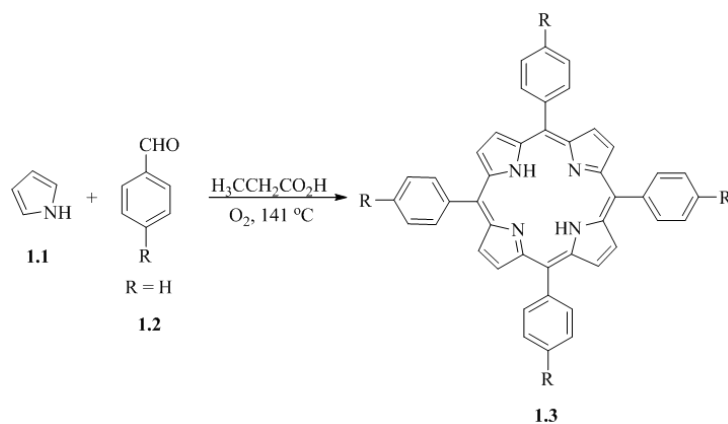
Scheme 1.2 Synthesis of TPP via Adler-Longo method.[18]

In 1987, Lindsey and coworkers concluded that TPP could actually be produced under equilibrium conditions. This synthetic strategy permits the formation of substituted porphyrins which were once unattainable via alternate routes.[18] The procedure was developed based on pyrrole **(1.1)** and benzaldehyde **(1.2)** reacting to form the thermodynamically favored product, tetraphenylporphyrinogen **(1.4)**, under specific reaction conditions (Scheme 1.3). Porphyrinogens are intermediates that convert irreversibly to aromatic porphyrins upon oxidation.
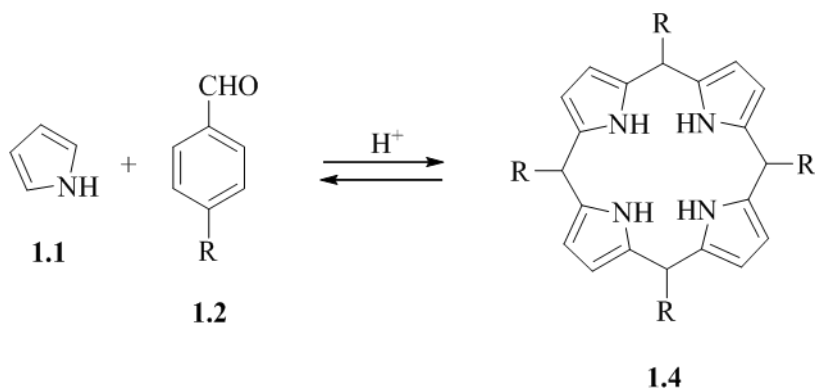
Scheme 1.3 Synthesis of pyrrole **(1.1)** and benzaldehyde **(1.2)** forming tetraphenylporphyrinogen **(1.4)** at room temperature.

Several factors of the Lindsey method contribute to porphyrin yields. For instance, the selection of acid catalyst and oxidant, starting material concentrations, reaction time, and presence of water in solvent can all influence the reaction.[21] The synthesis involved reacting

pyrrole **(1.1)**, benzaldehyde **(1.2)**, and triethyl orthoacetate in a dilute solution of anhydrous dichloromethane (DCM) at equimolar concentrations (10^{-2} M) (Scheme 1.4). An aliquot of a Lewis acid catalyst, such as $BF_3 \cdot Et_2O$ or TFA (10^{-3} M), is added to the reaction mixture and allowed to sit at room temperature for ~1 hour.
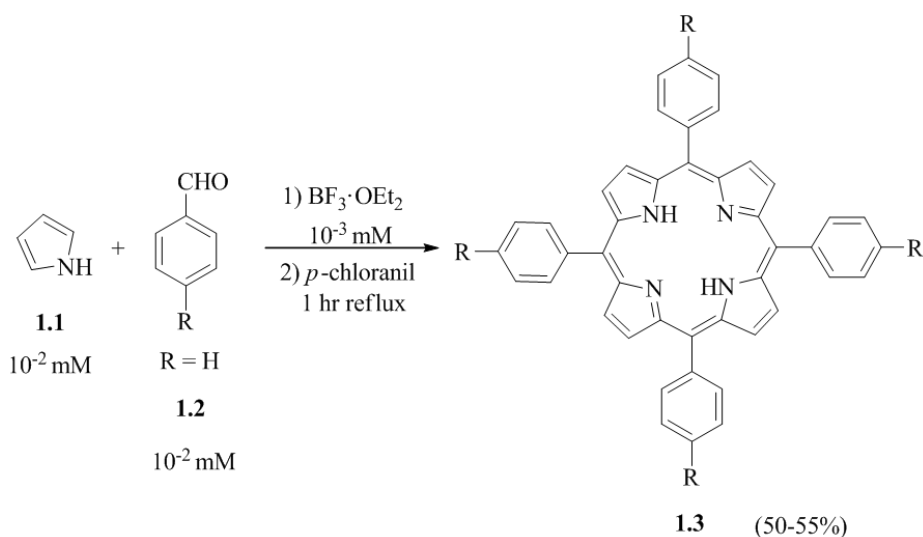
Scheme 1.4 Synthesis of TPP via Lindsey method.[18]

Once the reaction has reached equilibrium, the oxidant can then be added to convert the porphyrinogen intermediate to porphyrin. Oxidizing agents, *p*-chloranil or 2,3-dichloro-5-6-dicyanobenzoquinone (DDQ), are both useful for this conversion. Adding DDQ yields an immediate conversion of the intermediate. However, *p*-chloranil is a milder oxidant and requires at least an hour to completely react. Though the reaction time when using *p*-chloranil is longer, it produces a higher yield of porphyrin than DDQ. The final product is obtained in much higher yields (50-55%) and more substituents are tolerated, which is a great improvement with respect to previous methods.

1.4.2 UV-Vis and Fluorescence

A typical porphyrin has very intense Soret bands around 400 nm, which is a common characteristic of the macrocyclic conjugation.[5] However, as the porphyrins aggregate, their chemico-physical properties change. Different aggregates do not exhibit the same properties and as a result, spectroscopy can be vital to unraveling the self-assembly process. Fluorescence and absorption spectra were used to follow the kinetic aggregation routes of the protonated porphyrin species. Protonation is a diffusion-controlled process which is relatively much faster than aggregation, thus the study was experimentally possible.

H_2TPPP was dissolved in five 0.1 M phosphate buffer solutions at pH 5, 6, 7, 8, and 9 to examine the pH dependency and the aggregates that formed as a result. The concentration of the solutions was dilute (2.5 μM) in order to prevent any forced aggregation. Figure 1.7 shows the UV-Vis and fluorescence data which were acquired 1 hour after preparing the sample solutions.
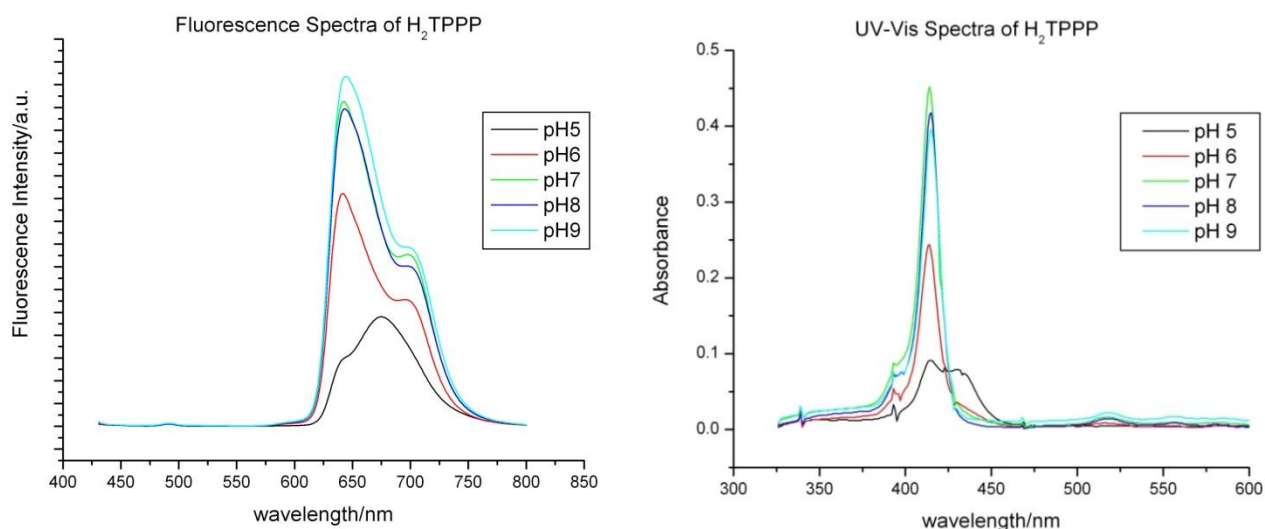
Figure 1.7 Fluorescence (left) and absorption (right) spectra of 2.5 μM H_2TPPP in phosphate buffer solutions at pH 5, 6, 7, 8, and 9 after allowing the samples to aggregate for 1 hour.

Based on the spectra, the emission and absorbance intensities varied for each pH which proved the pH dependence. According to the peaks of the fluorescence and absorption spectra, there are

at least two different species present in the pH 5 solution. Both of these thermodynamic products, in theory, can lead to aggregates that follow distinct kinetic aggregation pathways.

Peak profiles of H_2TPPP solutions at pH 6, 7, 8, and 9 appear to be exactly the same, and only vary by height (intensity). All the solutions possess an emission peak at ~650 nm and a Soret absorption band at ~420 nm which indicates the presence of one common monomeric species. The emission peak around 675 nm for the pH 5 solution is not present for any of the other pH solutions. The protonation equilibrium step for that particular monomer can only be achieved at low pH levels. These observations conveyed that at least three distinct protonated species were achieved within the prepared pH range.

The absorption band at ~438 nm for the pH 5 solution is a typical characteristic of porphyrin with the inner core protonated (Figure 1.7, black curve). In this form, TPPP is a zwitterionic species with a positively charged core and negatively charged peripheral phosphonate groups. It has been reported[22] that the N–H bonds at the center of the porphyrin ring adopt a saddle structure in the diacid, which facilitates hydrogen bonding with negatively charged peripheral groups of neighboring porphyrins. The electrostatic interaction between these charged regions is the driving force behind the self-assembly of J-aggregates. The formation of the aggregates became more apparent over a period time as they were allowed to self-assemble. After 2 days, a bathochromic shift (~420 to 425 nm) and increase in the Soret band of the pH 5 solution was noticed (Figure 1.8, UV-Vis). Such a shift is an indication of the formation of J-aggregates. Solutions at pH 6, 7, 8, and 9 appeared to exhibit minimal changes as a function of time. The emission and absorption spectra of H_2TPPP were monitored periodically over the course of 3 weeks (Figure 1.9). The intensities decreased as time increased, cause being due to self-quenching brought about by monomeric constituents forming aggregates
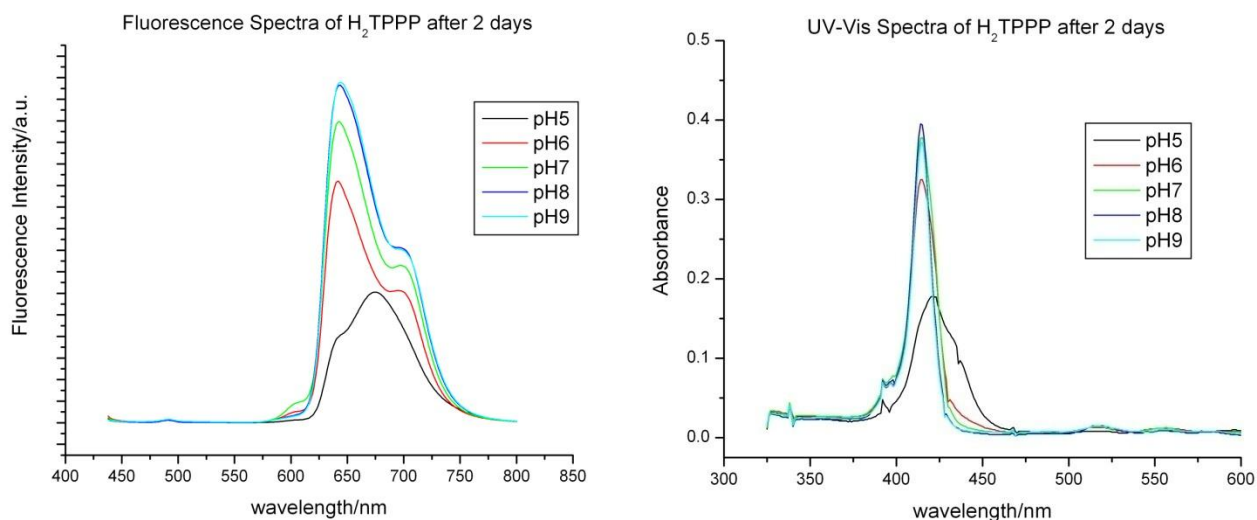
12

Figure 1.8 Fluorescence (left) and absorption (right) spectra of 2.5 μM H_2TPPP in phosphate buffer solutions at pH 5, 6, 7, 8, and 9 after 2 days.

In fact, the absorption band that was present at ~438 nm for the pH 5 solution diminished as a function of time. Based on this occurrence, it was concluded that the monomeric zwitterionic species followed the kinetic pathway to form J-aggregates as a function of time. It should be noted that the rate of self-aggregation was fairly slow. Days passed before noticing any major changes in the peaks of the spectra. The pH 8 and 9 solutions seemed to change the least over the entire monitoring period. This evidence implies that the monomeric species did not exhibit aggregation, and may be due to the induction of electrostatic repulsion. When the phosphonic groups are not protonated and the nitrogen atoms inside of the macrocycle core are also negatively charged, aggregation is then hindered. The emission peak intensity for solutions at pH 6 and 7 decreased drastically and their slight spectral shifts indicated J-aggregation. Similar to the solutions at pH 8 and 9, H_2TPPP at pH 5 showed some signs of minimal aggregation. Protonation of the nitrogens in the macrocycle core along with the phosphonate groups, incur positive charges. Thus, the self-assembly of the species is hindered by charge repulsions.
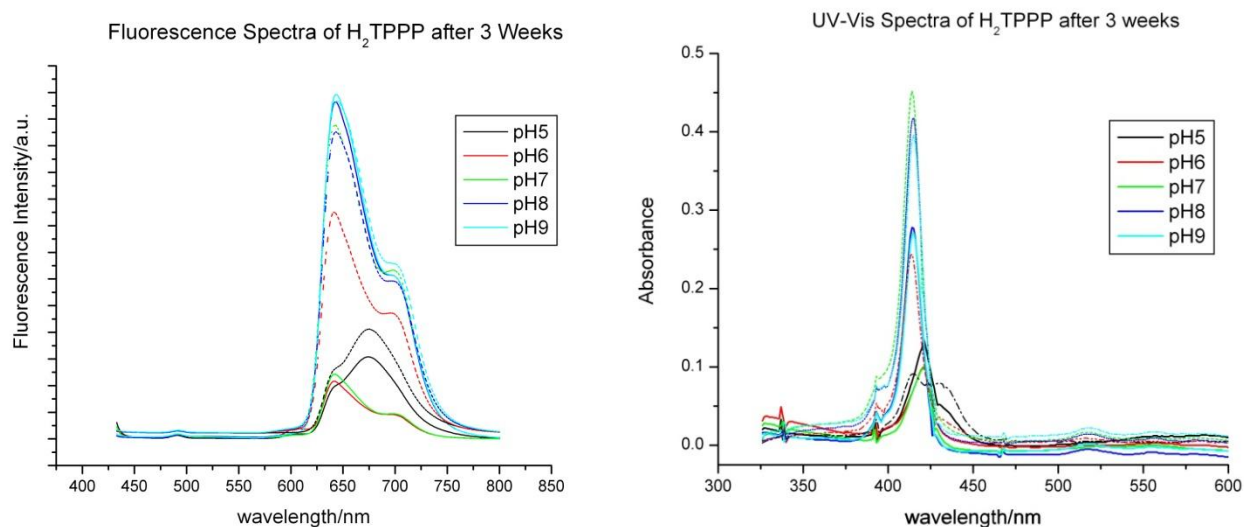
Figure 1.9 Fluorescence (left) and absorption (right) spectra of 2.5 μM H₂TPPP in phosphate buffer solutions at pH 5, 6, 7, 8, and 9 before (dashed) and after (solid) allowing samples to aggregate for 3 weeks.

A control experiment was performed to better discern the chemico-physical changes during the self-assembly process, which involved monitoring H_2TPPP in dimethylsulfoxide (DMSO) (Figure 1.10). Porphyrin aggregation is prevented in DMSO solution because, unlike water, it is an aprotic solvent. It is also a strongly coordinating solvent with both a "soft" and "hard" site located on the oxygen and sulphur atom, respectively.[22] Upon dissolving H_2TPPP in DMSO, the porphyrin molecules tend to coordinate to DMSO via hydrogen bonding rather than to each other. The oxygen atom of DMSO hydrogen bonds to the N–H groups inside the core of the porphyrin macrocycle. Detection of these hydrogen bonds can be obtained by observing a red shift in the Soret band (3-5 nm) and blue shifts of the Q-bands (2-4 nm) of the porphyrin in DMSO with respect to other solvents.[23] Unlike H_2TPPP, which is capable of following multiple aggregation pathways, H_2TPPS is limited to only one route.

UV-Vis and fluorescence spectra of H_2TPPS were collected and compared to H_2TPPP to distinguish the differences in their photophysical properties during self-assembly.

14

Figure 1.10 Fluorescence (left) and absorption (right) spectrum of H_2TPPP at a concentration of 1.0 μM in DMSO-d_6 after 1 hour.

As a result of the inner nitrogen atoms of H_2TPPS possessing a pK_a of approximately 4.8, the pH for the experiment ranged from 4 to 9. It was important to protonate the core nitrogens in order to facilitate the electrostatic interactions with the negatively charged sulfonate groups on the neighboring porphyrins. Consequently, these interactions are the driving forces that lead to self-aggregation.

As expected, the H_2TPPS solutions only formed one type of product as a function of pH. None of the variations that were observed for the spectra of H_2TPPP were noticed for H_2TPPS. According to the UV-Vis spectra, the peak profiles of solutions at pH 6 through 9 are identical with the exception of the very slight red shift for pH 6 (Figure 1.8). Two absorption peaks were observed for pH 5 solution. This phenomenon indicates the presence of a mixture of monomeric species[24]; H_2TPPS in free base form and the zwitterionic form. The mixture is a result of the close proximity to the critical pK_a of 4.8. The absorption peak at ~440 nm for pH 4 and 5 is attributed to J-aggregation based on the apparent bathochromic shift.

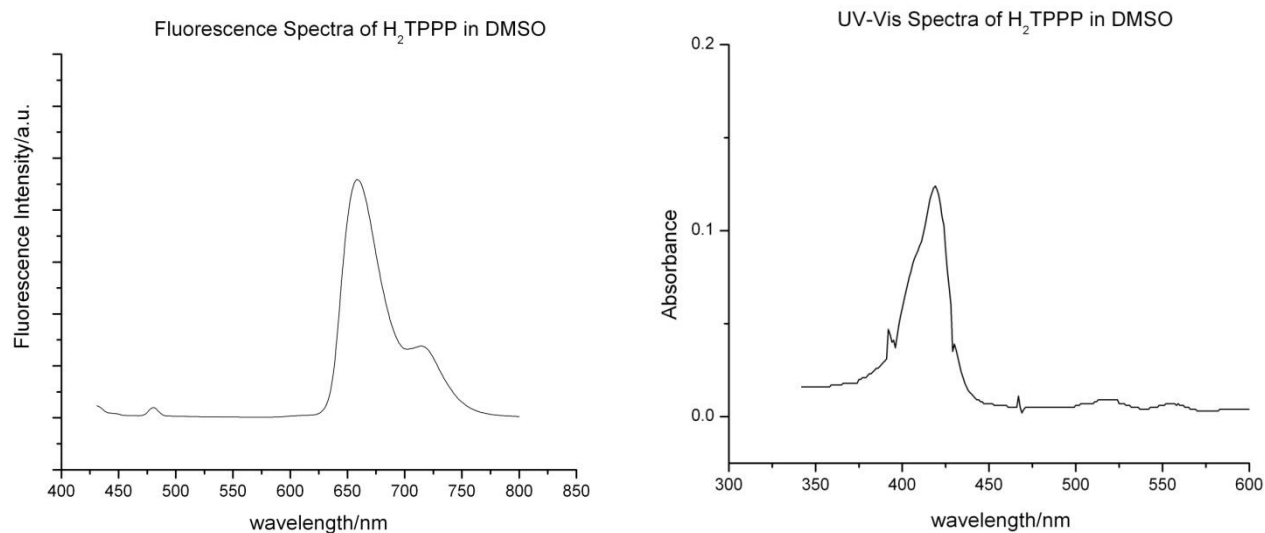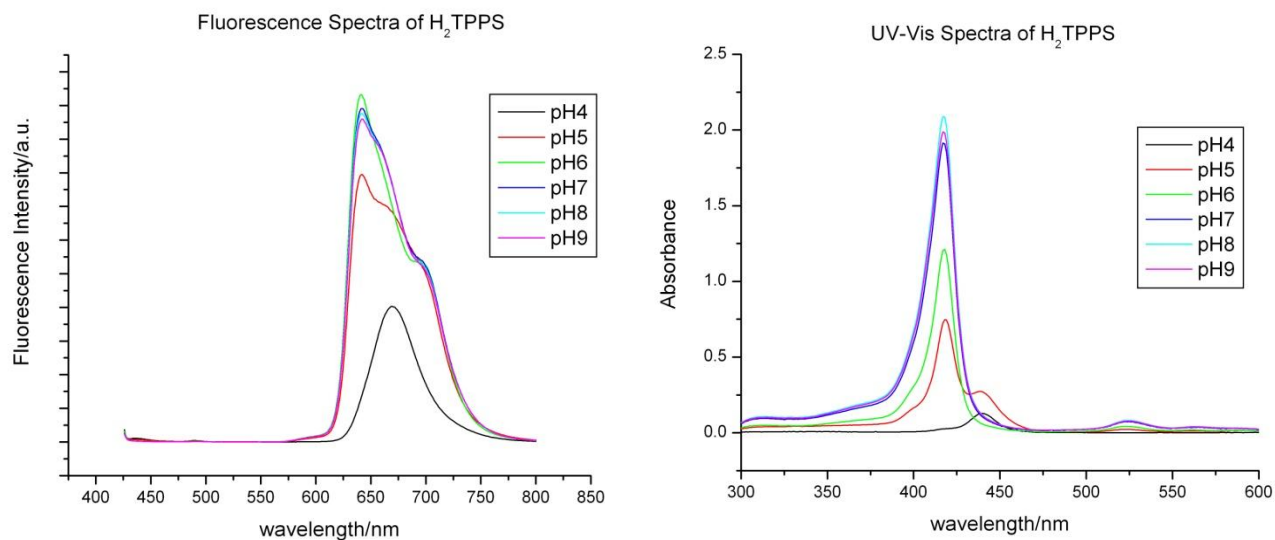**Figure 1.11** Fluorescence (left) and absorption (right) spectrum of 3.0 μM H$_2$TPPS in phosphate buffer solutions at pH 4, 5, 6, 7, 8, and 9 approximately 30 minutes after preparation.

1.5 Conclusion

Variations in the absorbance bands and peak intensities of the different pH solutions of H$_2$TPPP suggest that the self-assembly process is pH dependent. This dependency can be exploited to hierarchically control the architecture of the aggregates.

The UV-Vis spectra of the aggregated species in solutions at pH 5, 6, and 7 exhibited bathochromically shifted bands, which is a characteristic of J-aggregation or protonated species. However, the higher pH solutions seemed to show no signs of self-assembly but the slight hypsochromically shifted Soret bands suggest the formation of H-type complexes. Thus, it was concluded that H$_2$TPPP predominantly forms J-aggregates in aqueous solutions of low pH and H-aggregates at higher pH levels.

1.6 Future Work

The thermodynamic pathways of H$_2$TPPP were afforded by the presence of three protonation sites. In theory, each protonation step leads to a specific species that follows a

kinetic pathway to form distinct aggregates. To explore the potential for forming additional pathways, octaphosphonic acid-substituted phthalocyanines (Figure 1.12) will be examined. This compound possesses more protonation sites than H_2TPPP, which should ideally increase the number of potential protonated monomeric species in aqueous solution.
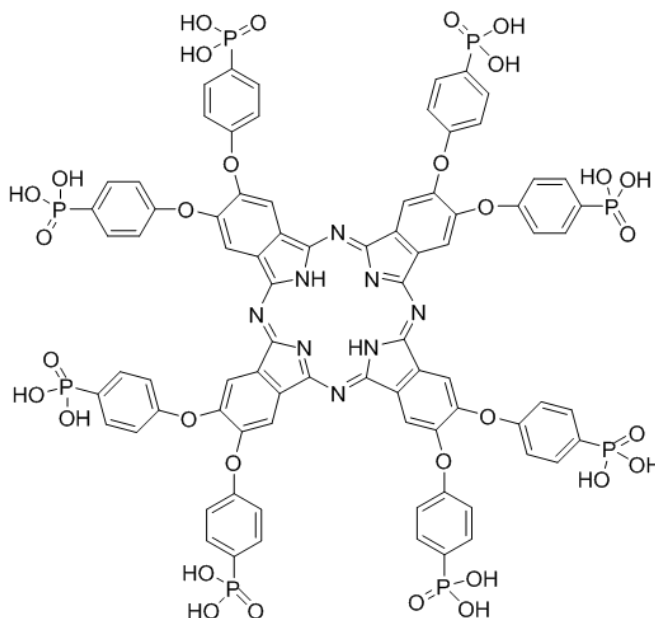
Figure 1.12 Structure of octaphosphonic acid-substituted phthalocyanine

1.7 General Experimental to Chapter 1

Meso-tetrakis(4-sulfonatophenyl) porphyrin (H_2TPPS) was obtained from Frontier Scientific. Diethyl(4-formylphenyl)phosphonate was purchased from Epsilon Chimie. All other solvents and reagents were obtained from Sigma-Aldrich and used without further purification. The pH of the buffer solutions was measured with a Fisher Scientific AR10 pH meter. Alumina gel (50-200 µm, neutral, standard activity I, Sorbent Technologies) was used for column chromatography. Analytical thin-layer chromatography (TLC) was carried out using polyester backed TLC plates (precoated, 200 µm) from Sorbent Technologies. NMR spectroscopy was performed on a DPX-250 Bruker spectrometer using deuterated DMSO as internal reference.

High resolution ESI mass spectra were obtained using an Agilent Technologies 6210 Time-of-Flight LC/MS.

1.7.1 Meso-tetrakis(4-phosphonatophenyl) porphyrin (H$_2$TPPP) Synthesis

Meso-tetrakis(4-phosphonatophenyl) porphyrin (H$_2$TPPP) was synthesized using the Alder-Longo method.[20] A solution mixture of 1.0 g of diethyl(4-formylphenyl)phosphonate, 0.27 mL of pyrrole, and 15 mL of propionic acid was added to a 50 mL round bottom flask. While under argon, the mixture was refluxed for approximately 1.5 hrs. Once complete, the dark brown solution was poured into a 1 L Erlenmeyer flask and placed in an ice bath for 10 min. Distilled water was saturated with sodium bicarbonate and added to the flask while stirring the mixture until the aqueous phase was neutralized (pH of ~8.0). The aqueous phase was then extracted with dichloromethane (DCM) several times and the organic phase was dried over anhydrous sodium sulfate. Following filtration, the DCM was removed via rotovaporation and a dark brown residue remained. The residue was purified by column chromatography on neutral alumina in a solvent system composed of dichloromethane-methanol (99:1). MS (ESI) m/z 1159.37 [M + H]$^+$

The product, meso-tetrakis(4-phosphonatophenyl) porphyrin octaethyl ester, was dissolved in 10 mL of dichloromethane and degassed with argon. Approximately 0.45 mL of bromotimethylsilane (TMSBr) was added with a microliter syringe. The green mixture was allowed to stir overnight at room temperature while covered. Completion of the reaction was indicated via TLC. Under reduced pressure, the solvent and TMSBr were removed. A solution of 1:1 H$_2$O/MeOH was added along with 0.5 mL of HCl to the reaction and was allowed 24 hours to stir. The desired product was washed with H$_2$O and dried under high vacuum. H$_2$TPPP was then characterized by NMR spectroscopy and mass spectroscopy (ESI).
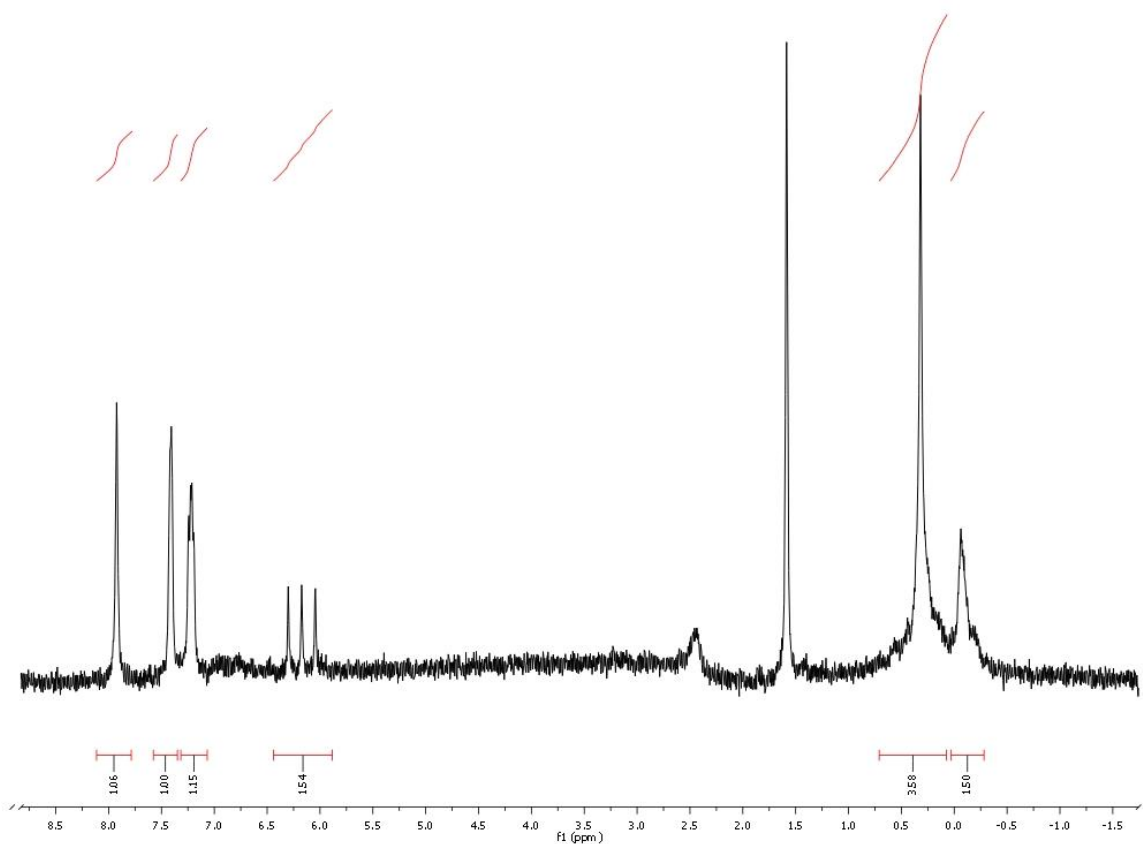
Figure 1.8 ^{1}H-NMR spectrum of meso-tetrakis(4-phosphonatophenyl) porphyrin (H$_2$TPPP) in deuterated DMSO at 250 MHz.

1.7.2 UV-Vis and Fluorescence

UV-Vis spectra were collected by means of a Pharmacia Biotech Ultrospec 4000 spectrophotometer in the range of 300-600 nm at room temperature with a 1.0 cm quartz cuvette. The concentration of the prepared H$_2$TPPP solutions was 2.5 μM in phosphate buffer solution. Fluorescence spectra were acquired with a Horiba Fluorolog Spectrofluorometer at room temperature in the range of 400-850 nm with a quartz cuvette.

The stock phosphate buffer solution was prepared by mixing di-sodium hydrogen phosphate dihydrate in deionized water to yield 0.1 M solution. Ortho-phosphoric acid 85% was added drop-wise to the solution while monitoring with a pH meter to obtain targeted levels.

1.8 References

1. Alzheimer's Association, 2008 Alzheimer's Disease Facts and Figures. June 2008 ed.; 2008; Vol. 4.

2. Drain, C. M.; Hupp, J. T.; Suslick, K. S.; Wasielewski, M. R.; Chen, X. *J. Porphyrins Phthalocyanines* **2002,** *6*, 241-304.

3. De Napoli, M.; Nardis, S.; Paolesse, R.; Vicente, M. G. H.; Lauceri, R.; Purrello, R. *J. Am. Chem. Soc.* **2004,** *126*, 5934-5935.

4. White, W. I.; Dolphin, D., *The Porphyrins*. Academic Press: New York, 1978; Vol. 5.

5. Smith, K. *Porphyrins and Metalloporphyrins*. Elsevier Scientific Publishing Company: Amsterdam, 1975.

6. Pandey, R. K.; Smith, K. M.; Dougherty, T. J. *J. Med. Chem.* **1990,** *33*, 2032-2038.

7. Dougherty, T. J.; Comer, C. J.; Henderson, B. W. *J. Nat. Cancer Inst.* **1998,** *90*, 889-905.

8. Vicente, M. G. H. *Curr. Med. Chem. -Anti-Cancer Agents* **2001,** *1*, 175-194.

9. Scherz, A.; Brandis, A.; Mazor, O.; Salomon, Y.; Scheer, H. *PCT Int. Appl.* **2004,** 56.

10. Lauceri, R.; Gurrieri, S.; Bellacchio, E.; Contino, A.; Monsu'scolaro, L.; Romeo, A.; Toscano, A.; Purrello, R. *Supramol. Chem.* **2000,** *12*, 193-202.

11. Drain, C. M.; Batteas, J. D.; Flynn, G. W.; Milic, T.; Chi, N.; Yablon, D.; Sommers, H. *Proc. Natl. Acad. Sci.* **2002,** *99*, 6498.

12. Freedman, L. D.; Doak, G. O. *Chem. Rev.* **1957,** *57*, 479-523.

13. Zayats, V. Y.; Lobanov, V. V.; Pinchuk, V. M. *Theor. Exp. Chem.* **1988,** *24*, 328-331.

14. Lauceri, R.; De Napoli, M.; Mammana, A.; Nardis, S.; Romeo, A.; Purrello, R. *Synth. Met.* **2004,** *147*, 49-55.

15. Tonizzo, A.; Cerminara, M.; Macchi, G.; Meinardi, F.; Periasamy, N.; Sozzani, P.; Tubino, R. *Synth. Met.* **2005,** *155*, 291-294.

16. Pradeep, T., H and J aggregates. Indian Institute of Technology Madras: 2007.

17. Knapp, E. W. *Chem. Phys.* **1984,** *85*, 73-82.

18. Lindsey, J. S.; Schreiman, I. C.; Hsu, H. C.; Kearney, P. C.; Marguerettaz, A. M. *J. Org. Chem.* **1987,** *52*, 827-836.

19. Rothemund, P. *J. Am. Chem. Soc.* **1936,** *58*, 625-627.

20. Adler, A. D.; Longo, F. R.; Finarelli, J. D.; Goldmacher, J.; Assour, J.; Korsakoff, L. *J. Org. Chem.* **1967,** *32*, 476-476.

21. Easson, M. Ph.D. Dissertation, Louisiana State University, Baton Rouge, LA, 2008.

22. Tran-Thi, T.-H.; Palacin, S.; Clergeot, B. *Chem. Phys. Lett.* **1989,** *157*, 92-96.

23. Agirtas, S.; Ion, R.-M.; Bekaroglu, O. *Mater. Sci. Eng., C* **2000,** *7*, 105-110.

24. Gandini, S. C. M.; Yushmanov, V. E.; Borissevitch, I. E.; Tabak, M. *Langmuir* **1999,** *15*, 6233-6243.

CHAPTER 2 ANALYTICAL ULTRACENTRIFUGATION: CHARACTERIZATION OF SOLUTION-STATE BEHAVIOR

2.1 Introduction

Analytical Ultracentrifugation (AUC) is a powerful technique used to characterize macromolecules in solution. It can provide a wide range of information about the thermodynamic and hydrodynamic properties of solutes in the native state, and directly measures their molecular weights.[1] AUC data is determined by sedimentation analysis which is based on thermodynamics. The thermodynamic parameters in equations that describe sedimentation behavior can all be acquired experimentally.[2]

When Nobel Prize Laureate Theodore Svedberg and co-workers developed the idea for the ultracentrifuge in 1923, it was solely intended for investigating colloidal systems.[3] However, AUC became most popular in the fields of biology and biochemistry. It was the first instrument to yield dependable molar mass values for biopolymers.[4] As technology advanced, new methods such as dynamic light scattering (DLS), size exclusion chromatography (SEC), and electron microscopy (EM) forced the AUC into extinction. In 1991, Beckman redesigned the AUC and introduced it as the Optima XL-A.[5] The new model influenced the rebirth of analytical ultracentrifugation, but the versatility of this method of characterization is seldomly exploited. AUC is a great tool for analyzing associating systems and is essential in this study for understanding the kinetic properties of the porphyrin aggregates.

The two basic types of AUC experiments are sedimentation velocity and sedimentation equilibrium. In principle, sedimentation equilibrium (SE) experiments are capable of providing information about the size of the individual molecules which form complexes, the size of the complex, the strength of subunit interactions and the thermodynamic nonideality of the solution.[2] Sedimentation velocity (SV) experiments can be used to study the molar mass, size distribution,

and shape of macromolecules.[6] SE and SV experiments can present complementary information and most studies require the application of both techniques to obtain useful data. For the purposes of this study, only SE experiments were performed and will be discussed further in the chapter.

2.2 Instrumentation and Experimental Applications

Ultracentrifugation is based on the application of a centrifugal field, $\omega^2 r$, where ω represents the angular velocity and r is the distance to the axis of rotation. The angular velocity ω (s^{-1}) is $2\pi/60$ multiplied by the number of revolution per minute (rpm), and the maximal speed is 60,000 rpm in the XLA. The radial distance r in the conventional cell is typically in the range of 5.8-7.2 cm (Figure 2.1). Ultracentrifuge cells are sector-shaped with the walls parallel to the radii of the rotor to minimize convection and prevent sedimenting particles from colliding with the walls (wall effects). It is also important for the cells to be durable and withstand the stresses of exceptionally high gravitational fields. A centrifugal force of up to 300,000 g can be achieved by the rotor system; g is the acceleration due to gravity, 9.81 $m \cdot s^{-2}$. Macromolecules that are exposed to such a great force will redistribute in solution.[7]
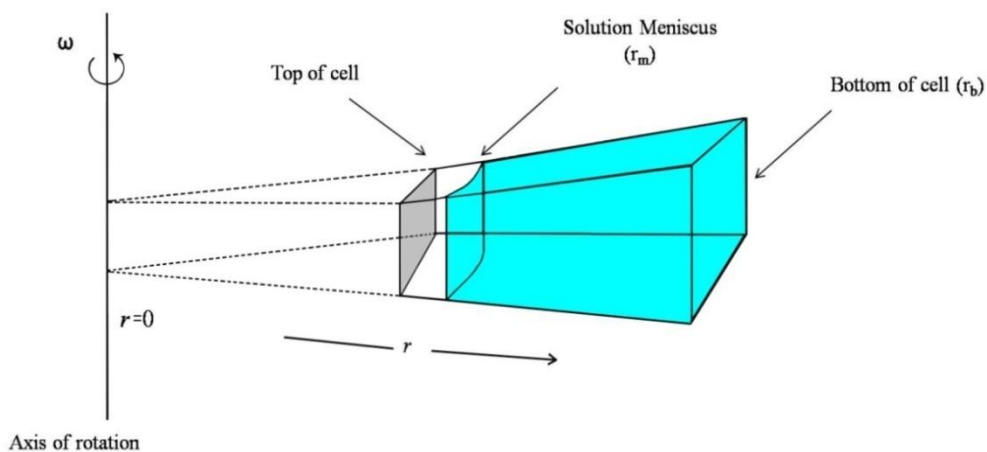
Figure 2.1 Schematic of a sector-shaped ultracentrifuge cell and its radial positions with respect to the axis of rotation corresponding to its position in the rotor.

An analytical ultracentrifuge is identical to a classic preparative ultracentrifuge with respect to their appearance. In fact, the only key component that distinguishes these instruments from one another is the optical system. An analytical device permits the measurement of particle distribution as a function of time via the determination of radial position during ultracentrifugation.[7] The two types of optical systems used for AU are the Optima XL-A which measures absorption, and XL-I which has supplementary Rayleigh interference optics. The addition of the Rayleigh interference system affords more sensitive optical detection of concentration distributions without the requirement of chromophores.[8] A chromophore typically occurs via conjugated pi systems or metal complexes. As mentioned in chapter 1, porphyrins are highly conjugated molecules, and thus the XL-I was not necessary for optical detection of the samples.

The Optima XL-A analytical ultracentrifuge uses a xenon flash lamp as the light source, which supplies a wavelength range of 190-800 nm. However, single-wavelength light is selected by a toroidally-curved diffraction grating. Light of other wavelengths are blocked and stray light is minimized by a series of absorbing filters. To account for the fluctuations in light intensity from pulse to pulse, a small amount of incident light from the diffraction grating is normalized by being reflected onto a detector located at an implicit focal point.

As the sample cell passes over the detector, monochromatic light is transmitted through the sector (sample or solvent) of interest. Regulation of the synchronized timing of the light flash (pulse) and rotor precessions is monitored by a reference magnet located in the base of the rotor. The maximum pulse rate is 100 flashes per second; one flash per ten revolutions at 60,000 rpm. The intensity of the transmitted light through the sample sector is measured with reference to the

solvent by a photomultiplier tube located beneath the rotor. A lens-slit assembly travels as a unit

to provide radial scans of the sectors (Figure 2.2).[9]
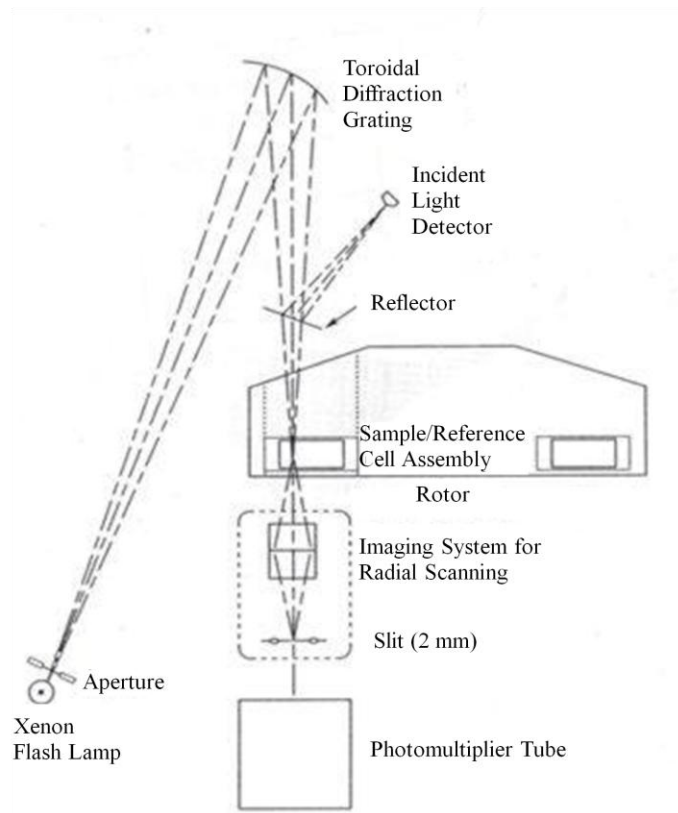
Figure 2.2 Schematic diagram of the Beckman Optima XL-A system.[9]

2.3 Theory

The foundation for understanding the theory of sedimentation processes in the

ultracentrifuge begins with the derivation of flow (or flux) equations. These equations describe

the isothermal mass transport of thermodynamic components in a centrifugal field. A simple

kinetic theory approach can be applied to derive a useful flow equation for a system consisting of

a homogenous solute and a solvent (binary solution). Such an approach suggests that transport of

solute molecules through the solvent is the result of a centrifugal force, a buoyant force, and a

diffusion force.[10] On the contrary, as the concept developed, it was noted that the kinetic theory

had to be replaced by nonequilibrium (irreversible) thermodynamics in order to obtain the general and rigorous derivation of flow equations for the ultracentrifuge.[11] The simpler mechanical point of view will be described within the scope of the chapter.

According to Van Holde, most phenomena such as sedimentation and diffusion share a common feature: A system *not* in equilibrium migrates towards equilibrium. In route to equilibrium, it is inevitable for flow to occur. For instance, a molecule moving with a velocity Δv in time Δt across a surface s in an ultracentrifuge cell will travel a distance $\Delta x = v\Delta t$. As a result, every solute molecule within a slab of the cell returning to this distance from the surface s will pass through s in Δt sec. The amount of molecules passing is the concentration times the slab volume $\Delta w = Cs\Delta x$, which can also be written as $\Delta w = Csv\Delta t$ (Figure 2.3). Hence, flow is defined as $J = \Delta w / s\Delta t$.[12] Because of this relation between flow and molecular velocity, the definition of flow can be expressed in simpler terms as

$$J_i = v_i C_i \qquad (1)$$

where flow J_i is the uniform concentration C_i of component i crossing 1 cm^2 of surface in 1 sec with a velocity v_i.
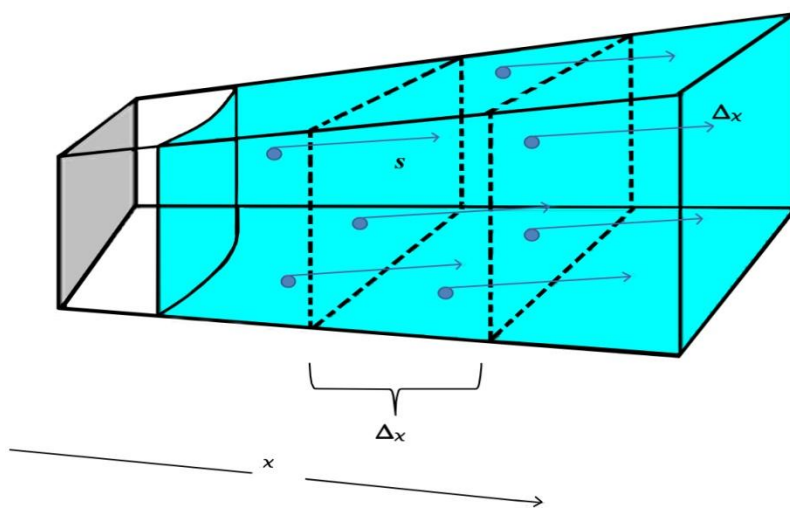
Figure 2.3 Illustration of flow and molecular transport velocity, and their relativity in an ultracentrifuge cell.

The concept of transport processes, with respect to sedimentation, is based on three forces acting on the solute molecules; centrifugal force, buoyant force, and frictional force (Figure 2.4). For instance, a molecule in solution inside a rapidly spinning rotor with an angular velocity ω, is subjected to a centrifugal force F_c. This force experienced by the molecule is proportional to its mass (m) and distance (r) from the axis of rotation. Therefore, the centrifugal force can be defined as $F_c = \omega^2 rm$. Concurrently, a counter force is produced as a result of the molecule displacing some solution, inducing a buoyant force $F_{buoy} = -\omega^2 rm_0$; where m_0 is the mass of the displaced solution. Lastly, as the molecule flows with a velocity v as a result of the previously mentioned forces, it incurs a viscous drag from the solvent. The drag causes the molecule to resist its flow through solution. This resistance is the frictional force F_d and is expressed as $F_d = -fv$, where f is the frictional coefficient.[12]
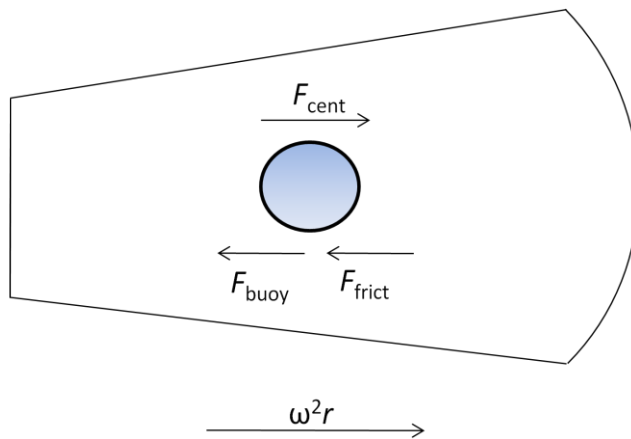
Figure 2.4 Illustration of the forces experienced by a particle inside a sector-shaped cell during subjection to a centrifugal field.

Sedimentation equilibrium experiments use an angular velocity comparable to the forces of diffusion which prevents the macromolecules from completely sedimenting to the cell bottom. This approach distributes the molecules in a stable concentration gradient along the radial dimension of the cell. Knowledge of the thermodynamic terms involved in the sedimentation

transport process can be used to derive information about the molecular weights, states of aggregation, and association constants of macromolecules in solution.[13]

## 2.4 Determination of Average Molecular Weight

Most techniques used for obtaining molecular weights of polymeric materials are not capable of yielding accurate values when detecting heterogeneity. However, the analytical ultracentrifuge is able to overcome such a limitation. In fact, the AU is most renowned for its ability to combine measurements of sedimentation and diffusion coefficients for the determination of molecular weights. When sedimentation and diffusion reaches a state of equilibrium, in theory, apparent movement of the solute no longer occurs; it is maintained as long as the rotor speed and temperature are held constant. Based on the Lamm equation, the equilibrium concentration distribution (c_r) is a function of the buoyant molecular weight, $M(1 - \bar{v}\rho)$; angular velocity, ω^2; and temperature, T in Kelvin.[14]

$$\frac{\ln(c_r)}{r^2} = \frac{M(1-\bar{v}\rho)\omega^2}{2RT}$$
(2)

where M is the monomer molar mass, $\bar{v}$ is the partial specific volume, ρ is the density of the solvent, and R is the gas constant. As a result of the concentration distribution being dependent on the buoyant molecular weight, accurate values of the $\bar{v}$ and ρ are imperative for determining the molecular weight using the SE method. For the investigated porphyrins, H_2TPPP and H_2TPPS, the calculated partial specific volume $\bar{v}$ was approximately 0.85 cm^3·g^{-1}. The solvent was water, which has a density ρ of 0.9982 g·cm^{-3} at 20 °C.

For an ideal system, a ln(c_r) vs r^2 plot yields a straight line with a slope proportional to M (Figure 2.5). In the case of an associating system, such as the self-assembly of porphyrin aggregates, the plot is not capable of yielding a straight line; requires more intense analysis. The plot tends to curve upward when the sample material undergoes aggregation. This same

curvature can also occur when there is a mixture of materials of varying molecular weights or the sample experiences degradation.[15] When the plot curves downward, it indicates the solution being non-ideal. The tangents to the curve of a nonlinear $\ln(c_r)$ vs r^2 plot yields the weight-average molecular weight for the varying species at each radial position.[14]

Plot of ln (c) vs r^2
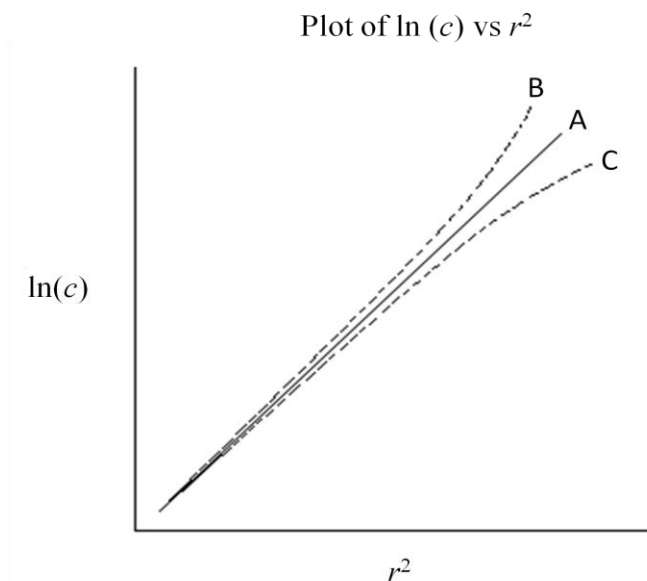
Figure 2.5 Plot of $\ln(c)$ vs r^2 showing curves from an (A) ideal solution (homogeneous); (B) polydispersed (heterogeneous) solution; and (C) non-ideal solution.

2.5 Results and Discussion

Based on results mentioned in chapter 1, the porphyrins H_2TPPS and H_2TPPP formed J- and H-aggregates in aqueous solution as a function of pH. Sedimentation equilibrium AUC was used to determine the size and association properties of these aggregates. Results from the SE analysis were fitted to models according to the ideal behavior of the components and were further studied.

An appropriate rotor speed is typically chosen by using a selection chart based on the known approximate molecular weight of the sample (Figure 2.6).[14] However, the size of the aggregates was unknown and initial guesses were required as a result. Such cases typically involve observing the solute redistribution at several rotor speeds until equilibrium is reached.
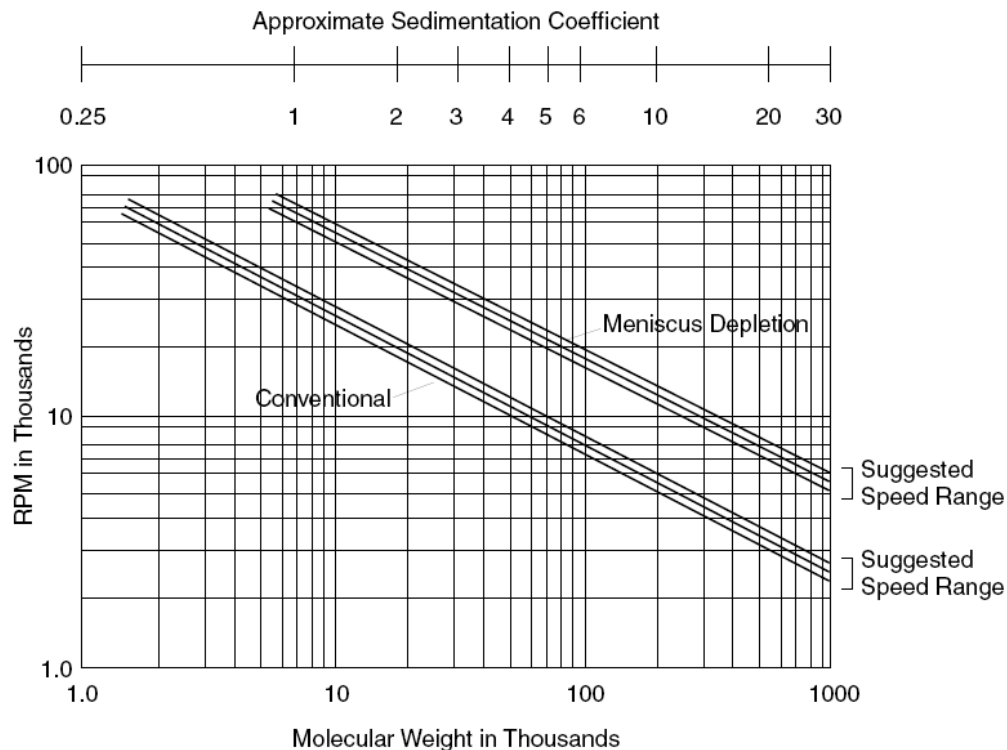
Figure 2.6 Illustration of the Rotor Speed Selection Chart used for sedimentation equilibrium runs. The conventional curve correlates rotor speed to either molecular weight or sedimentation coefficient. The meniscus depletion curve is the overspeed which is used for detecting the presence of low-molecular weight contaminates.[14]

Using a trial and error approach, the first assigned rotor speed was 16,000 rpm. Starting with a sufficiently low speed allows the centrifugal force to be small enough to permit an adequate opposing force of diffusion. At 16,000 rpm, the process of diffusion was greater than the process of sedimentation for all the samples. According to the absorbance *vs.* radius plots, H$_2$TPPS at pH 4 was the closest to reaching equilibrium; an early sign of large aggregates being present (Figure 2.7). The estimated average molecular weight obtained from the fitted results of H$_2$TPPS modeled as a single ideal species (Ideal 1), was $4,946.6 \pm 120.1$ g·mol^{-1}. However, the approximated value was absolutely inaccurate at 16,000 rpm because equilibrium conditions were yet to be achieved.
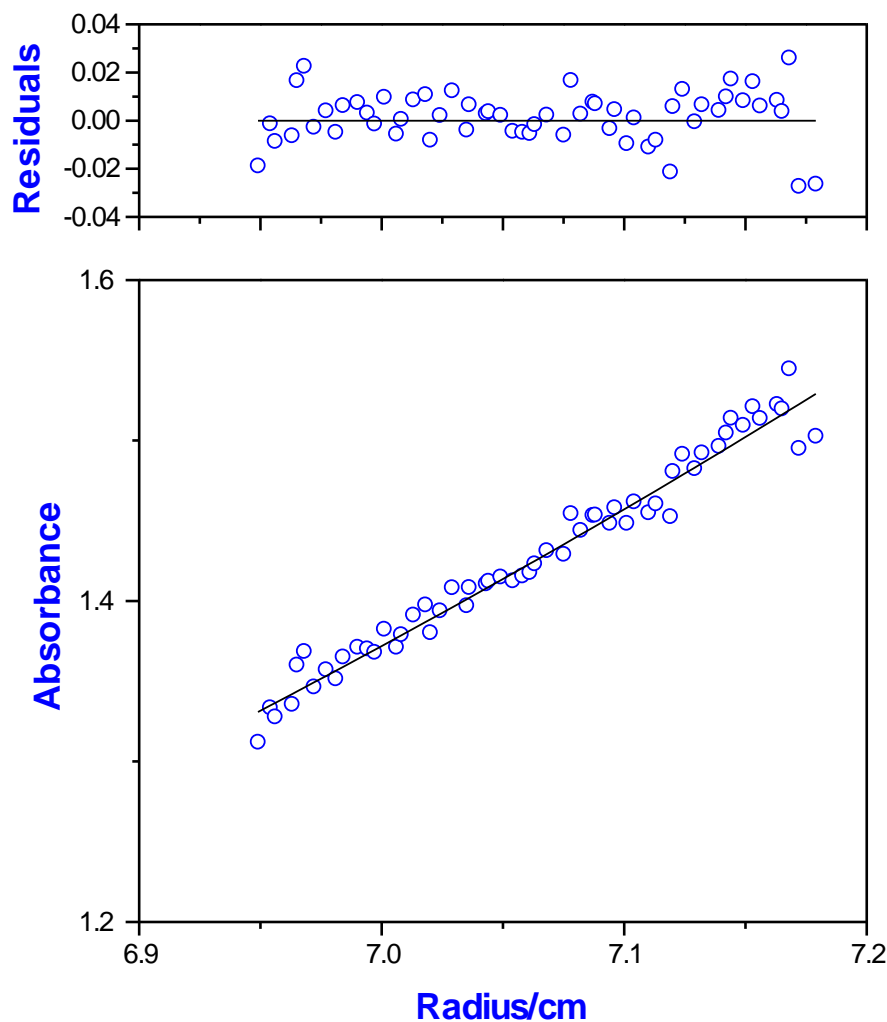
Figure 2.7 Absorbance *vs.* Radius plot of H_2TPPS in aqueous solution at pH 4 with a rotor speed of 16,000 rpm.

H$_2$TPPP at pH 5 subjected to a speed of 16,000 rpm exhibited relatively more diffusion (Figure 2.8). Small particles require higher speeds in sedimentation equilibrium experiments. The average molecular weight of the aggregates according to the Ideal 1 model fit was 3,947.4 $\pm$ 135.4 g·mol^{-1}. The molecular weight of H$_2$TPPP is ~1,159.4 g·mol^{-1}. The formation of trimers is suggested, but the agreement is inexact. This suggests a distribution of aggregates.
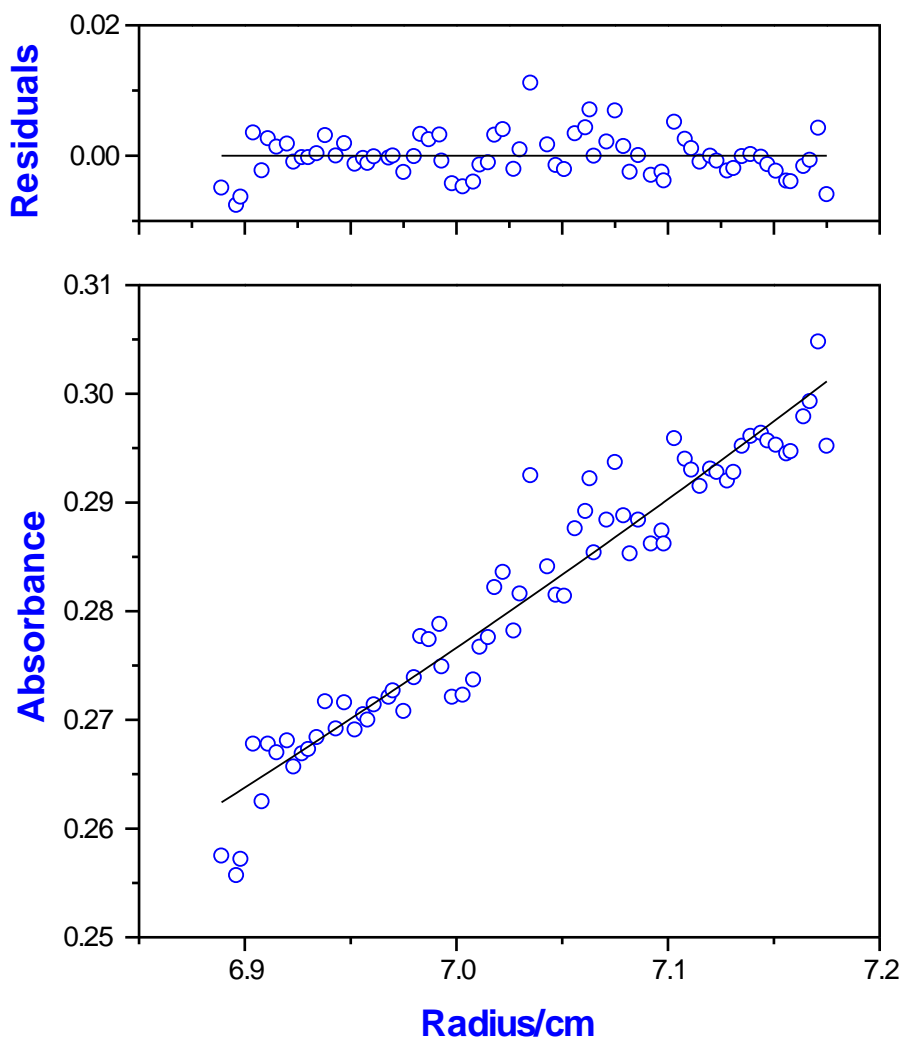
Figure 2.8 Absorbance *vs.* Radius plot of H$_2$TPPP in aqueous solution at pH 5 with a rotor speed of 16,000 rpm.

As expected, H$_2$TPPS at pH 9 was the farthest from sedimentation equilibrium at 16,000 rpm (Figure 2.9). From chapter 1 results, no signs of aggregation were observed for the porphyrins in solution at high pH levels. The Ideal1 model fit yielded an average molecular weight of 2,233.1 ± 243.7 g·mol^{-1}. The molecular weight of H$_2$TPPS is ~1,007.22 g·mol^{-1}. Hence, the calculated molecular weight suggests that dimers are formed at pH 9, but the implication remained inconclusive until further equilibrium experiments were conducted.

Figure 2.9 Absorbance *vs.* Radius plot of H₂TPPS in aqueous solution at pH 9 with a rotor speed of 16,000 rpm.

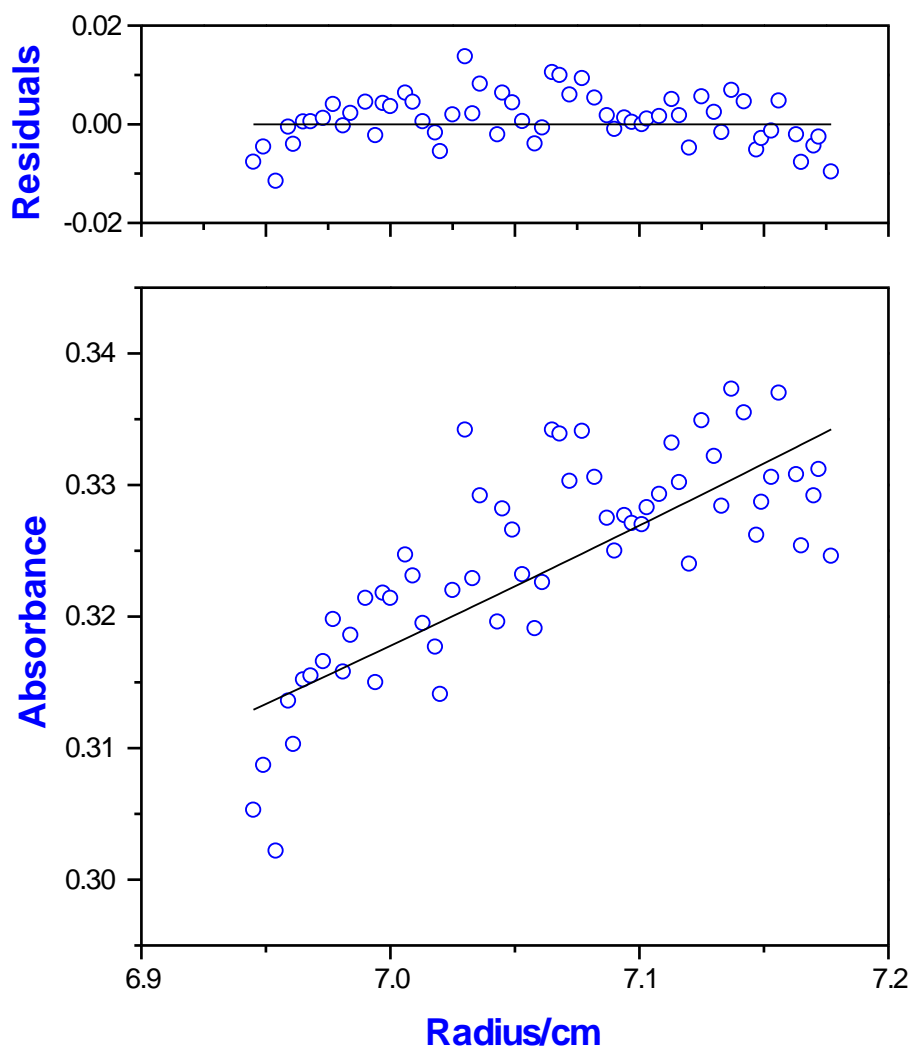Based on the Absorbance *vs.* Radius plots, the rotor speed was not fast enough to ensure competition between diffusion and sedimentation. To account for this, a relatively faster speed of 25,000 rpm was applied. More information was received for H₂TPPS at pH 4 under the newly acquired equilibrium gradient (Figure 2.10). For instance, the presence of two components was detected by the best fit model (Ideal 2). The increased angular velocity of the rotor provided greater partial fractionation, thus revealing the heterogeneity in the solution. Also, a systematic pattern for the residuals from the best-fit curve indicated an aggregating system. The calculated

average molecular weight for component 1 and component 2 was Mw_1=131,150 ± 64,290 g·mol^{-1} and Mw_2= 4,611.8 ± 131.9 g·mol^{-1}, respectively.
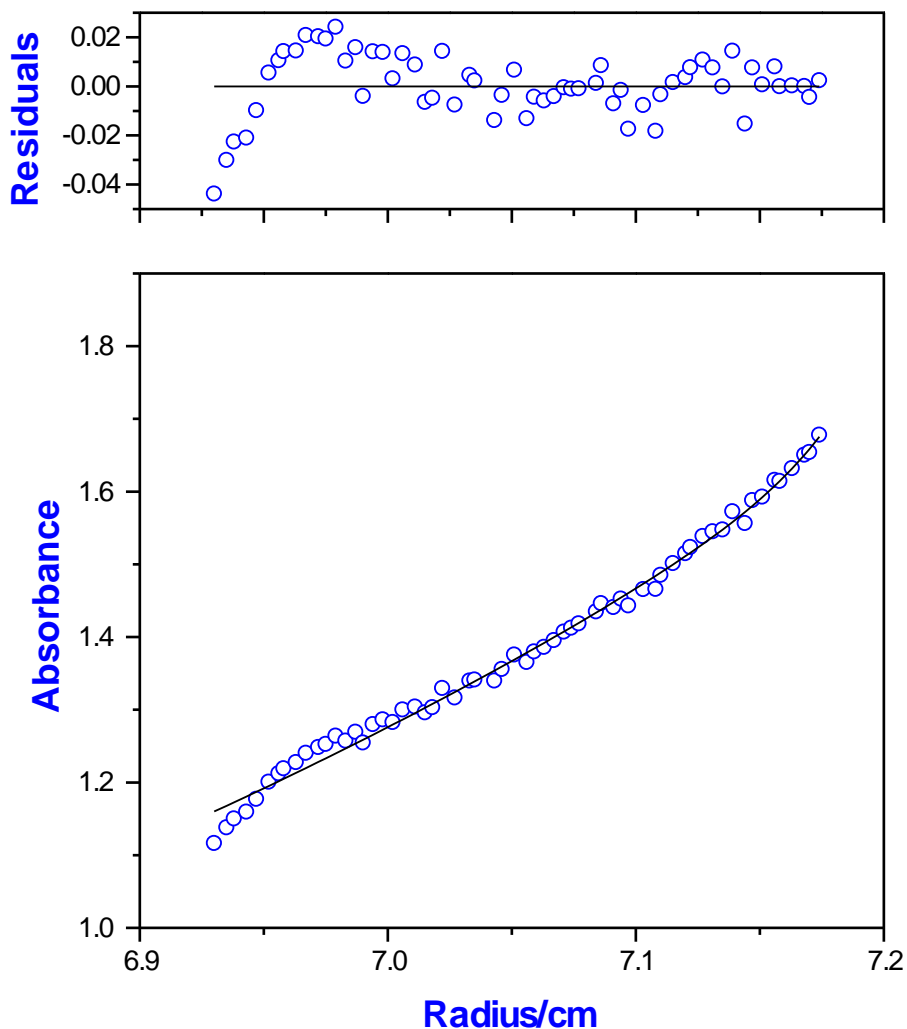
Figure 2.10 Absorbance *vs.* Radius plot of H_2TPPS in aqueous solution at pH 4 with a rotor speed of 25,000 rpm.

Although the rotor speed was increased to 25,000 rpm, the diffusional force was still much greater than the centrifugal force for H_2TPPP in solution at pH 5 (Figure 2.11). The average molecular weight was 3,513.1 ± 69.38 g·mol^{-1}, which is fairly close to the obtained value at 16,000 rpm. Also, the calculated uncertainty decreased as the system moved towards equilibrium.

34
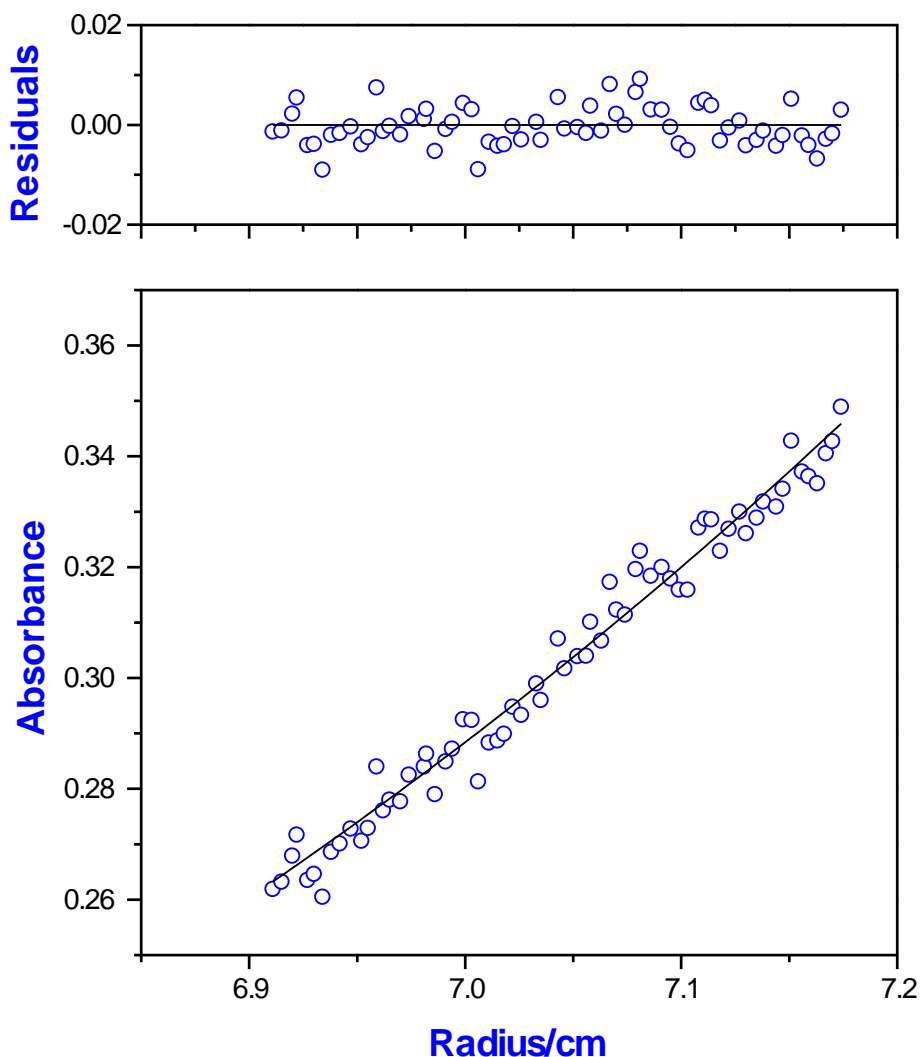
Figure 2.11 Absorbance *vs.* Radius plot of H_2TPPP in aqueous solution at pH 5 with a rotor speed of 25,000 rpm.

A poor equilibrium gradient was still prevalent for H_2TPPS in solution at pH 9 for the increased rotor speed (Figure 2.12). The average molecular weight of the aggregates acquired from the Ideal 1 fit was $2,787.5 \pm 130.5$ g·mol^{-1}. The possibility for dimer and trimer formation in pH 9 solution was confirmed at 25,000 rpm but not validated until examined with a greater angular velocity. The final sedimentation equilibrium experiments were performed at a speed of 45,000 rpm. All the samples yielded well-defined curves for the Absorbance *vs.* radius plots

Assuming sedimentation and diffusion forces to be equivalent, the equilibrium gradients were further analyzed.

Figure 2.12 Absorbance *vs.* Radius plot of H_2TPPS in aqueous solution at pH 9 with a rotor speed of 25,000 rpm.

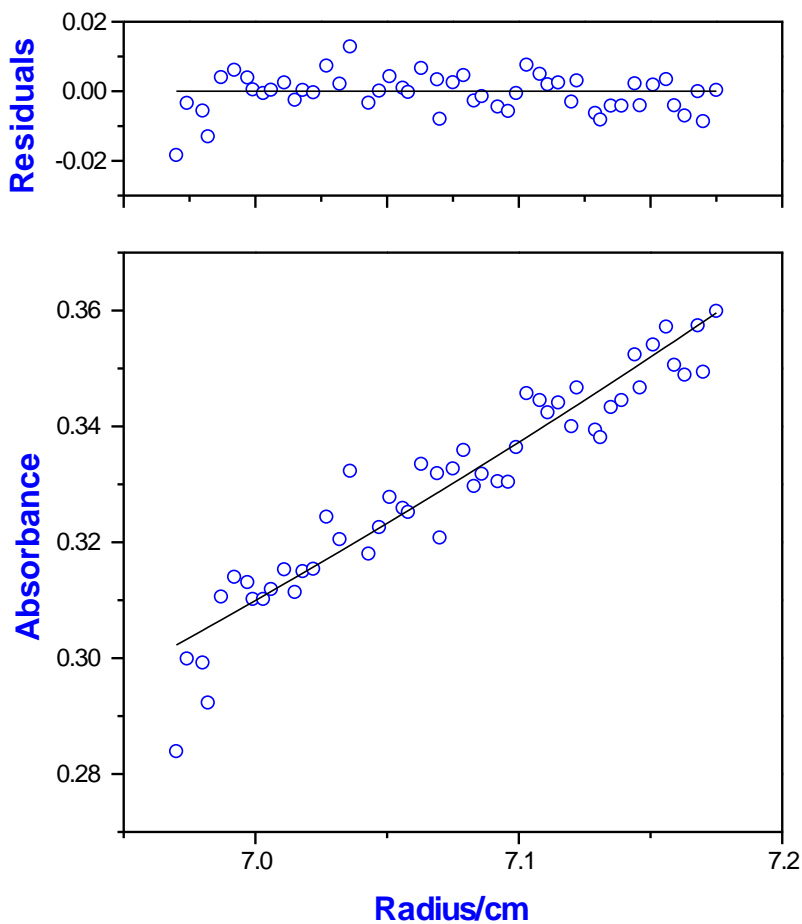For the first step, the absorbance vs. radius plot (equilibrium gradient) was transformed into a $M_{w,app}$ *vs.* concentration plot. The transforming method involves measuring the slope ($M_{w,app}$) of a segment of data points (typically 10-40) in a $\ln(c)$ vs. r^2 plot across the radial path one data point at a time. Data obtained from this transformation provides information concerning the associative order of the system. For an associating system, the plot curves upward as the

concentration increases. The second step involved simply searching for patterns in the residuals from the best-fit curves. A residual pattern not only provides insight into the behavior of the system, but also confirms the $M_{w,app}$ vs. concentration plot.

According to the best fit model (Ideal 2), the average molecular weights for H_2TPPS in solution at pH 4 were $Mw_1=25,397.9 \pm 3,153$ g·mol^{-1} and $Mw_2=3,054.1 \pm 74.65$ g·mol^{-1} for components 1 and 2, respectively (Figure 2.13). Component 1 is attributed to the formation of
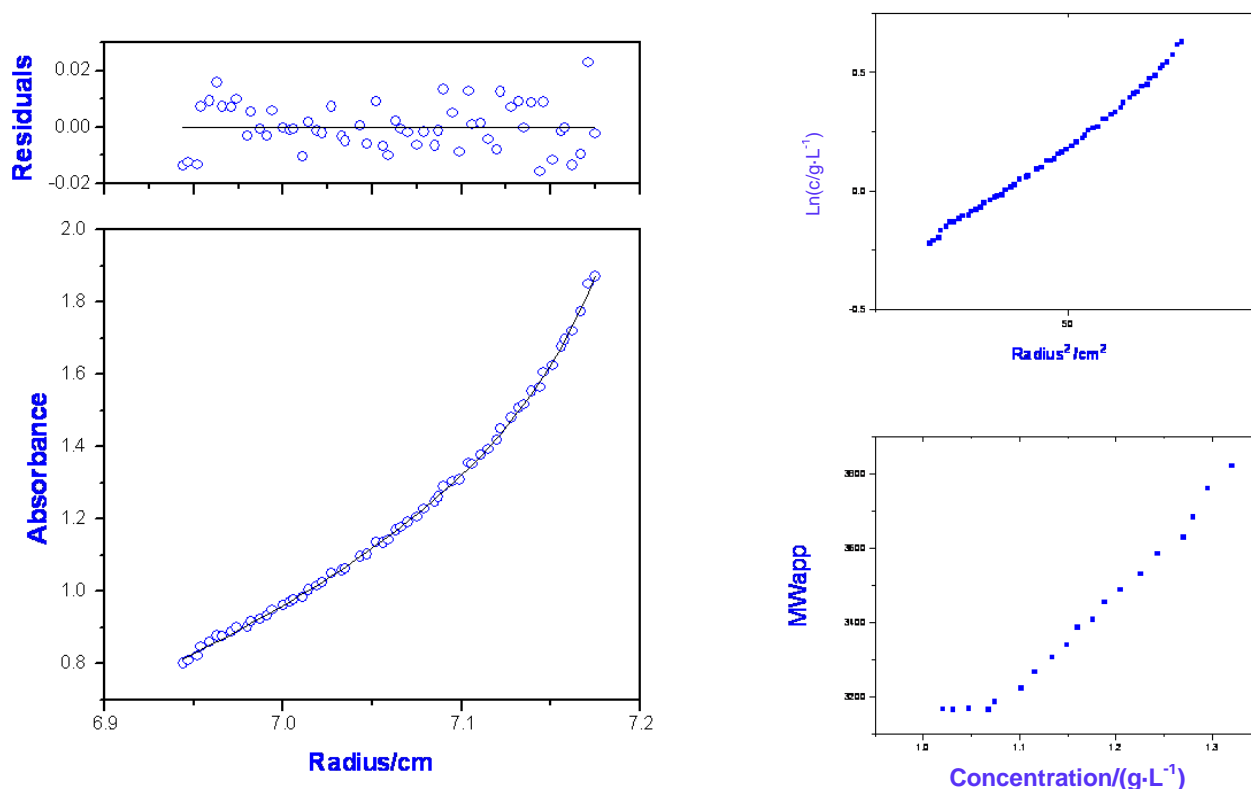
Figure 2.13 Sedimentation equilibrium analysis of H_2TPPS in solution at pH 4. The self-association behavior is denoted by the curve of the ln(c) *vs.* r^2 and $M_{w,app}$ *vs.* Concentration plots.

large aggregates, whereas component 2 are porphyrins complexed as dimers. The $M_{w,app}$ increased linearly as a function of concentration, further affirming the self-assembly process.

The diagnostics for complexity in H_2TPPP at pH 5 yielded unexpected results. The assumption was that the associative behavior would be identical to that displayed for H_2TPPS in low pH solution. However, the $\ln(c)$ *vs.* r^2 plot for H_2TPPP curved downward, which is a general characteristic of a non-ideal solution (Figure 2.14). The $M_{w,app}$ *vs.* concentration curve initially appeared to increase linearly, indicating signs of self-association. The upward trend eventually ended and then began to descend. The calculated average molecular weight was 2,970.9 $\pm$ 28.5 g·mol^{-1}. Perhaps H_2TPPP at pH 5 is indeed aggregating, but at a relatively slower rate than H_2TPPS.
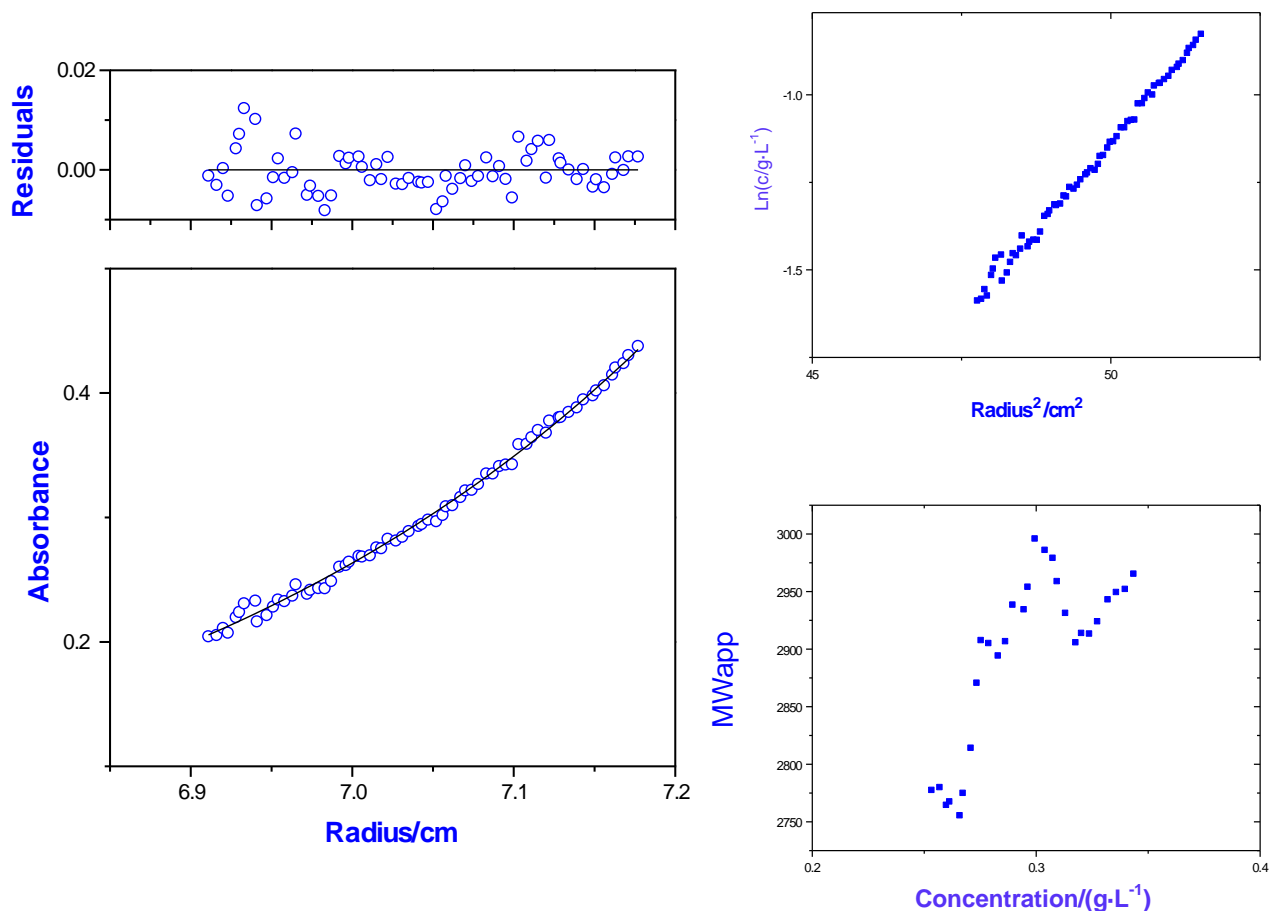
Figure 2.14 Sedimentation equilibrium analysis of H_2TPPP in solution at pH 5. The self-association behavior is denoted by the curve of the $\ln(c)$ *vs.* r^2 and $M_{w,app}$ *vs.* Concentration plots.

38

The data for H$_2$TPPS at pH 9 and H$_2$TPPP at pH 5 were each fitted to a model that assumed single component behavior (Ideal 1). Due to the electrostatic repulsions of the porphyrins at such high pH levels, no large aggregates were observed; only small dimers were formed. The calculated average molecular weight of the H$_2$TPPS dimers was Mw=2,731.3 ± 46.7 g·mol^{-1}. A plot of M$_{w,app}$ vs. concentration was generated to confirm the presence of a single species. For materials exhibiting behavior as single ideal species, M$_{w,app}$ does not vary with concentration,[14] however, the plot fluctuated (Figure 2.15). This observation proved that self-assembly was indeed occurring at high pH levels.

Figure 2.15 Sedimentation equilibrium analysis of H$_2$TPPS in solution at pH 9. The self-association behavior is denoted by the curve of the ln(c) vs. r^2 and M$_{w,app}$ vs. Concentration plots.
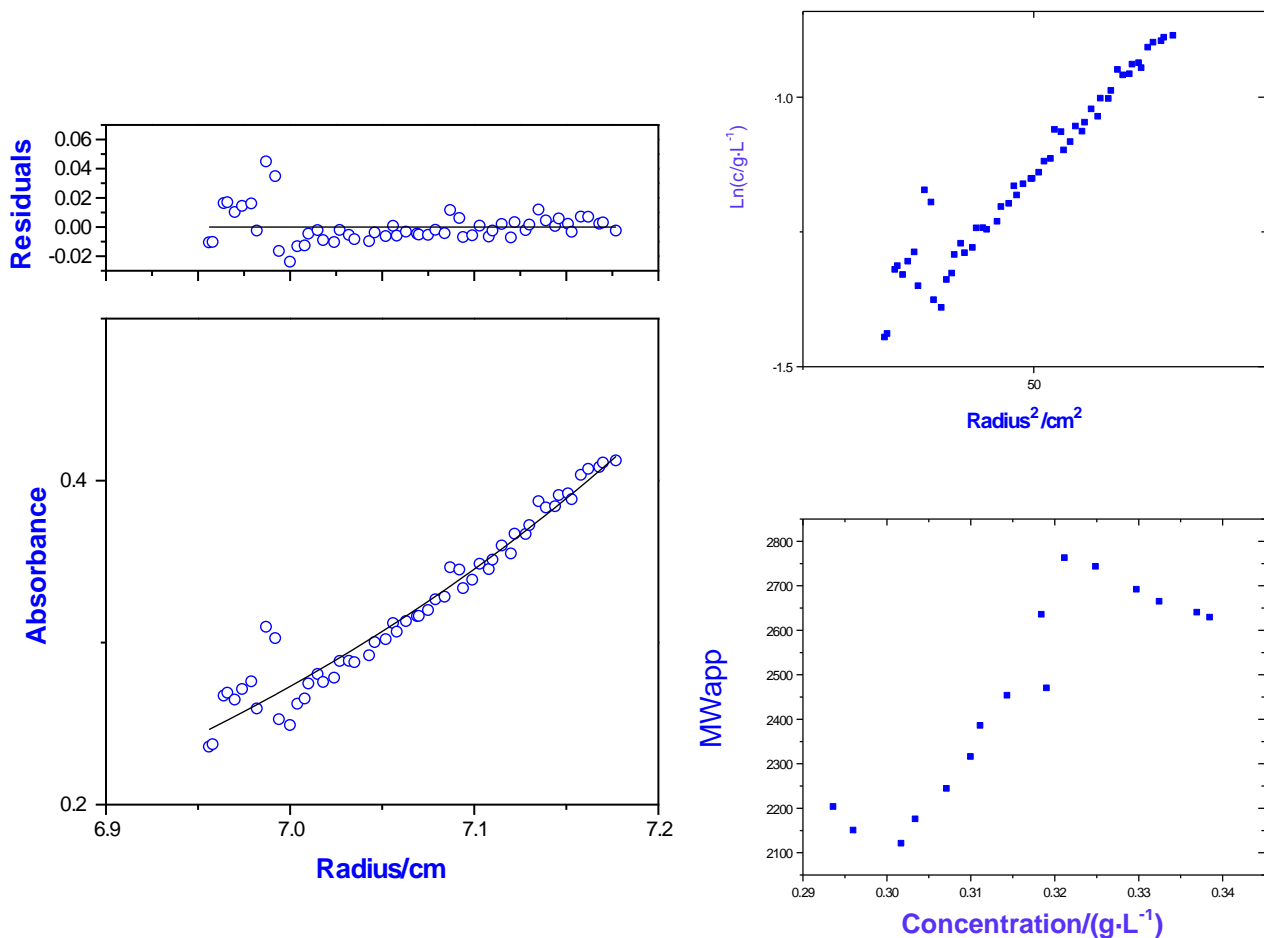
2.6 Conclusion

As expected, the porphyrins H_2TPPS and H_2TPPP at lower pH levels displayed the most aggregation. H_2TPPS at pH 4 formed the largest aggregates (Mw_1=25,397.9 ± 3,153 g·mol^{-1} and Mw_2=3,054.1 ± 74.65 g·mol^{-1}), whereas H_2TPPP at pH 5 was only 2,970.9 ± 28.5 g·mol^{-1}. The hypothesized reasoning for this occurrence is due to the rate of aggregation being much faster for the porphyrin with the substituted sulfonate groups. H_2TPPS is restricted to one self-assembly pathway, but multiple pathways exist for H_2TPPP. The competing aggregate formations of H_2TPPP may limit the rate of assembly. Another possible explanation involves the electrostatic interactions of the protonated phosphonic groups and the protonated interior nitrogens. The repulsion between the positive charges may hinder the aggregation process.

The obtained weight average molecular weight for the H2TPPS solution at pH 9 appeared to be consistent for all the runs at different rotor speed; Mw = 2,731.3 ± 46.7 g·mol^{-1}. Thus, it was concluded that these monomeric species formed dimers and trimers at high pH levels.

2.7 Experimental to Chapter 2

2.7.1 Sedimentation Equilibrium Procedures

Sedimentation equilibrium experiments were conducted using a Beckman Optima XL-A analytical ultracentrifuge. Epon charcoal-filled double-sector cells were assembled then loaded accordingly; 125 μl of solvent (phosphate buffer) in reference sector and 110 μl of 2.5 μM porphyrin in phosphate buffer solution in the sample sector. Weights were screwed into the counterbalance to adjust it equal to or at least 0.5 g less than the weight of the filled sample cell. The cell assembly was inserted into a four-hole rotor and the temperature inside the chamber was allowed to equilibrate at 20 °C while under vacuum. The best absorbed wavelength from the preliminary wavelength scan of the samples was 424 nm. Sedimentation equilibrium was

attained at 45,000 rpm over a time span of 24 hrs. All attained data was analyzed using the Origin Equilibrium software program.

2.7.2 Calculation of Partial Specific Volume

The partial specific volume was acquired using the *ab initio* calculation method of Durchschlag and Zipper.[16] The sum of the partial molar volume increments for each atom and atomic group in the investigated porphyrins yielded the partial specific volumes. This method is based on Traube's additivity principle and concept of volume increments for atoms. The calculated values are typically within a range of $\pm 2\%$ of the experimental value.

2.8 References

1. Svedberg, T.; Pedersen, K. O. *The Ultracentrifuge*. Clarendon Press: Oxford, 1940.

2. Ralston, G. B. *Introduction to Analytical Ultracentrifugation*. Beckman Instruments, Inc.: Palo Alto, Calif., 1993.

3. Svedberg, T.; Rinde, H. *J. Am. Chem. Soc.* **1924,** *46*, 2677.

4. Schachman, H. K. *Ultracentrifugation in Biochemistry*. Academic Press: New York, 1959.

5. Mächtle, W.; Börger, L. *Analytical Ultracentrifugation of Polymers and Nanoparticles*. Springer: New York, 2006.

6. Stafford, W. F. *Anal. Biochem.* **1992,** *203*, 295-301.

7. Ebel, C., Analytical Ultracentrifugation State of the Art and Perspectives. In *Methods in Protein Structure and Stability Analysis*, Nova Publishers: 2007.

8. Byron, O.; Harding, S. E. *Eur. Biophys. J.* **1997,** *25*, 305-306.

9. Furst, A. *Overview of Sedimentation Velocity for the Optima™ XL-A Analytical Ultracentrifuge*. Beckman Instruments, Inc.: Palo Alto, Calif., 1991.

10. Fujita, H. *Foundations of Ultracentrifugal Analysis*. Wiley-Interscience: New York, 1975; Vol. 42.

11. Hooyman, G. J. Thermodynamics of Irreversible Processes in Rotating Systems. Thesis, University of Leiden, Leiden, 1955.

12. Van Holde, K. E.; Johnson, W. C.; Ho, P. S. *Principles of Physical Biochemistry*. Pearson/Prentice Hall: Upper Saddle River, 2006.

13. Richard, A. J. Dissertation, Louisiana State University, Baton Rouge, LA, 2008.

14. McRorie, D. K.; Voelker, P. J. *Self-Associating Systems in the Analytical Ultracentrifuge*. Beckman Instruments, Inc.: Palo Alto, Calif., 1993.

15. Chervenka, C. H. *A Manual of Methods for the analytical utlracentrifuge*. Spinco Division of Beckman Instruments, Inc.: Palo Alto, Calif., 1973.

16. Durchschlag, H.; Zipper, P. *Prog. Colloid Polym. Sci.* **1994,** *94*, 20-39.

CHAPTER 3 SMALL ANGLE X-RAY SCATTERING: STRUCTURAL MODEL OF AGGREGATION

3.1 Introduction

Information about the type of aggregates is obtainable via UV-VIS spectroscopy. However, unlike scattering experiments, UV-VIS is not capable of providing information about the aggregate size and shape. The aim of scattering experiments is to determine the structure and organization of "particles" dispersed in solution. In this case, the generic term "particle" refers to dispersed matter, such as colloids, macromolecules, micelles or aggregates in a solvent.[1] Small angle scattering (SAS) is a common technique for examining structures in the range of 10 Å or larger.[2] This method provides structural information directly from systems possessing density inhomogeneities. In fact, the ability to analyze the inner structure of disordered systems is the most captivating feature of the SAS method.

The sources of radiation that can be used for SAS include light, x-rays, and neutrons. Each source has advantages and disadvantages, depending on the sample. For instance, particles in the size range of 5 to 300 Å can be explored by small angle x-ray or neutron scattering experiments, while those in the range of 100 to >3000 Å by light scattering.[1] However, light scattering is not capable of examining optically opaque samples and x-ray scattering exhibits difficulties in studying thick samples. Neutrons are electrically neutral particles, and therefore capable of penetrating almost anything but they can induce energy transfer effects due to neutrons interacting with the nucleus itself. Although each scattering technique has different features, in essence all of them are complementary.[3] In this work, the aggregate morphology of H_2TPPP and H_2TPPS in aqueous solution is studied via small angle x-ray scattering (SAXS) experiments.

Initially, dynamic light scattering was employed to study the size of the aggregates but the photosensitivity of the porphyrins made the task difficult. The samples fluoresced intensely, which interfered with the scattering signal. This occurrence was perhaps due to the wavelength of the light source (blue laser) being ~488 nm, which is in the range of excitation for porphyrins. SAXS then became a crucial technique for characterizing the structure of the porphyrin aggregates in solution. One advantage of using x-rays is fluorescence effects are negligible. X-rays are electromagnetic radiation which interacts with electric charges in matter.[4] The wavelength of x-rays range from approximately 10^{-2} to 10^{2} Å. The electromagnetic radiation of x-rays used to study materials occupies the range of 0.5-2.5 Å in wavelength. This angular range contains information about the shape and size of macromolecules, characteristic distances of partially ordered materials, pore sizes, and other data.[5]

3.2 Theory

Scattering experiments involve emitting well-collimated radiation of wavelength λ through a sample and measuring the variations of the small scattered intensity as a function of the scattering angle θ (Figure 2.1).[1] Upon interaction, coherent scattering patterns are generated from electron density inhomogeneities within the particle system.
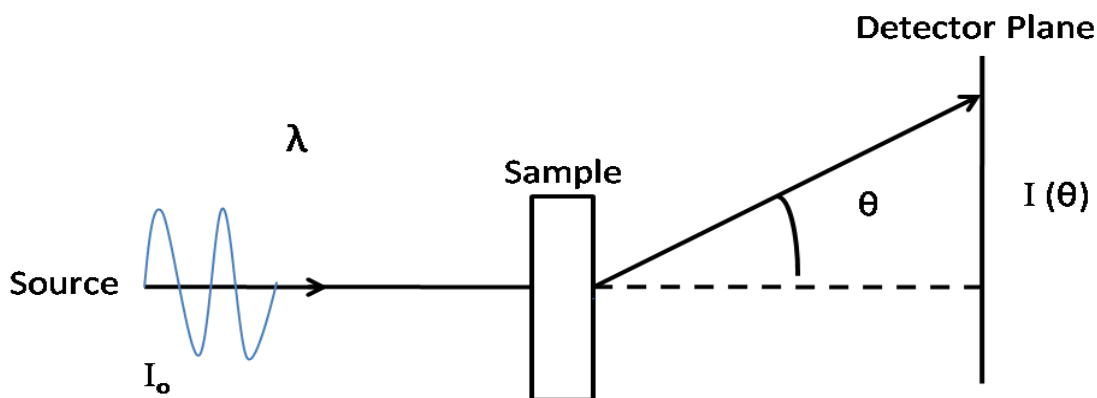
Figure 3.1 Schematic of general scattering experiment measuring the variations in intensity as a function of θ (scattering angle)

The scattering vector, q, is the parameter that characterizes the scattering geometry and is written as

$$q = \frac{4\pi}{\lambda} \sin\frac{\theta}{2}, \qquad (1)$$

where λ is the wavelength in the sample. The magnitude of q is related to the scattering angle θ, which is the angle between the incident beam and detector. The unit for q is inverse length (Å^{-1}).

Scattering processes are based on a law of reciprocity. A scattering curve $I(q)$ can be produced for a particle of any shape by Fourier inversion of the pair-distance distribution function, $p(r)$, where r is the distance between two scattering centers inside the particle.[6] In relation to the equation $q = 2\pi/d$, scattering vector q corresponds to reciprocal space and is inversely proportional to the distance d between scattering pairs in real space. By exploiting these parameters, a plethora of structural detail and information can be obtained from the scattering curve using various plots for analysis.

3.3 Scattering of Dilute Particulate System

In the dilute particulate system, individual particles of one material are uniformly dispersed in a matrix of a second material. For adequately dilute concentrations, the individual particles are positioned far apart from each other and as a result, are uncorrelated. The scattered waves from these different particles will be incoherent. Due to the lack of phase coherence, the overall intensity is basically the sum of the intensities of independently scattered rays from individual particles.[4]

The SAXS intensity, $I(q)$, provides information about the size and shape of the particles and can be represented by

$$I(q) = k\,N_p\,P(q)\,S(q), \qquad (2)$$

where k is the calibration factor, N_p is the scattering particle number density, $P(q)$ is the particle form factor, and $S(q)$ is the structure factor. For dilute systems, the structure factor is negligible ($S(q) \approx 1$) and the measured scattering cross section only depends on the particle form factor $P(q)$.[7]

When studying dilute solutions via SAXS, it is advantageous to use a strong synchrotron source. A synchrotron is capable of accelerating a beam of electrons to virtually the speed of light. The flux of x-rays emitted can be far greater than that obtained with conventional x-ray tubes, which minimizes the acquisition time for any single measurement.[4] The feasibility of retrieving informative scattering data from extremely weak scatterers is improved greatly by this application.

3.4 Determination of Radius of Gyration

In terms of dilute polymer solutions, small angle x-ray scattering can be expressed as

$$\frac{KC}{I(q,C)} \approx \frac{1}{M_w}\left(1 + \frac{q^2 \langle R_g{}^2 \rangle}{3}\right) + 2A_2 C \tag{3}$$

where K is the instrument constant related to the electron density; C is the concentration of the polymer in solution; A_2 is the second virial coefficient; and $\langle R_g{}^2 \rangle^{1/2} \equiv R_g$ is the radius of gyration. If K is known, the scattering data can be analyzed using a Zimm plot to determine R_g and A_2 by a simultaneous extrapolation to $q = 0$ and $C = 0$, respectively.[8]

The radius of gyration of a scattering body can also be estimated simply from the slope of the linear region of the Guinier plot [ln ($I(q)$) vs. q^2]; the initial slope gives $R_g^2/3$.[9] Even if the shape of the particle is unknown or irregular, the scattering function still obeys the expression

$$I(q) = \rho_0^2 v^2 \exp\left(-\frac{1}{3}q^2 R_g^2\right) \tag{4}$$

where $I(q)$ is the independent scattering intensity by a particle; ρ_0 is the average scattering length density in the particle; and v is the particle volume. Equation (4) is referred to as the Guinier law. The validity of the Guinier approximation is limited to scattering angles where q is sufficiently smaller than $1/R_g$. In addition, the system must be dilute to observe independent scattering from the particles and the solvent has to be of constant density.[4]

3.5 Results and Discussion

Scattering is primarily influenced by the particle concentration and size. Consequently, the prepared sample concentrations were dilute to prevent any forced assembly and crowding effects. The difficulty of analyzing the porphyrin solutions under the required conditions was taken into account by using a synchrotron source. The conducted SAXS experiments still encountered challenges in yielding meaningful scattering data for the aggregates. An explanation for this occurrence was insufficient x-ray flux, which was evident in the low scattering rates. Several experimental and instrumental parameters were adjusted throughout this study to improve the scattering measurements and will be discussed in further detail.

The initial sample concentration was 2.5 μM to be consistent with the experimental conditions in the previously mentioned chapters. However, absolutely no scattering was seen at this extremely low concentration. As a result, it was necessary to increase the concentrations to ~2 mM.

A scattering detector image of H_2TPPS at pH 4 is illustrated in Figure 3.2. Recall from Chapter 2 that the largest aggregates were formed in this solution, yet very little scattering was observed. The total acquisition time was approximately 5 hrs, scattering at a rate of 40.5 cts/s. To compensate for the lack of x-ray flux and obtain more counts, much longer runs are required. SAXS experiments on the solvent (background) alone were performed to measure its

contribution to the overall scattering intensity of the porphyrin solution. The obtained background scatter was subtracted off to extract the scattering from the aggregates.
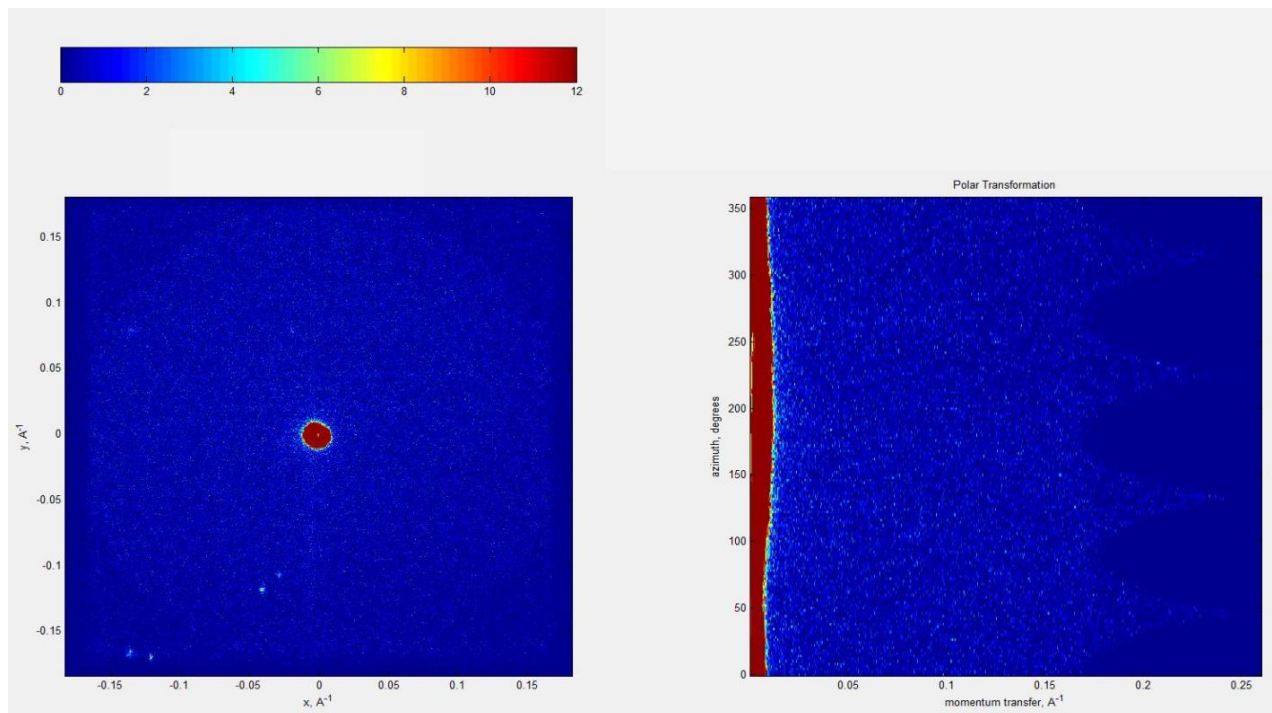

Figure 3.2 A 2-Dimensional scattering detector image (left) of H_2TPPS and its polar transform (right). The polar transformation provides a vertical interpretation of the omnidirectional detector image.

Figure 3.3 shows the experimental data obtained for H_2TPPS at pH 4 using this subtraction method. The profile of the scattering curves for the sample and the background were almost identical. In fact, some regions in the background curve showed more signs of scattering than the actual sample. Consequently, a large amount of noise was seen in the reduced curve. A possible reason for this phenomenon is low electron density contrast between the water (solvent) and the sample. Contrast variation aids in determining the composition of the aggregates because it utilizes the distinct scattering length densities of different atoms.[10] H_2TPPP in solution at pH 5 was expected to scatter less x-rays than H_2TPPS at pH 4, but the outcomes were very similar. Even after performing a background subtraction, the scattering intensity from the sample was

overwhelmed by the statistical variations (Figure 3.4). The first minimum was difficult to recognize without a great deal of uncertainty. All the suspected oscillation peaks dissipated as the scattering vector increased. Valuable information is suspected of being present in the scattering intensity curves, but is buried deep within the noise.
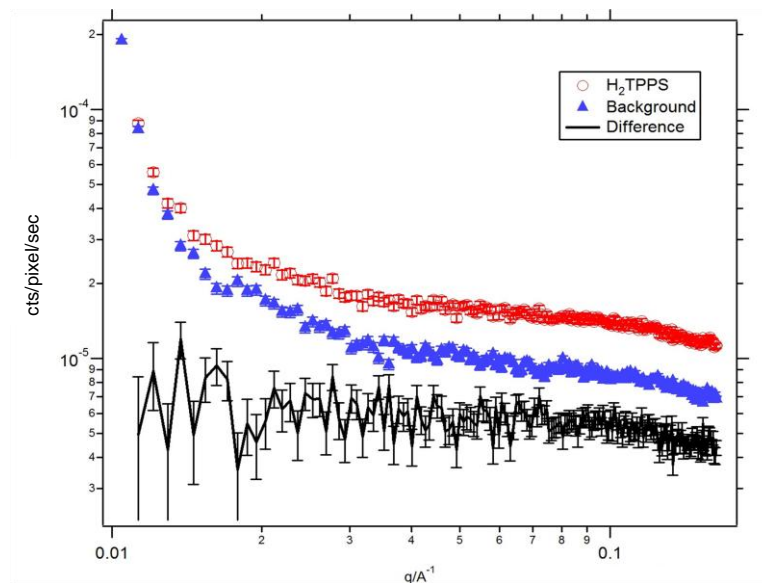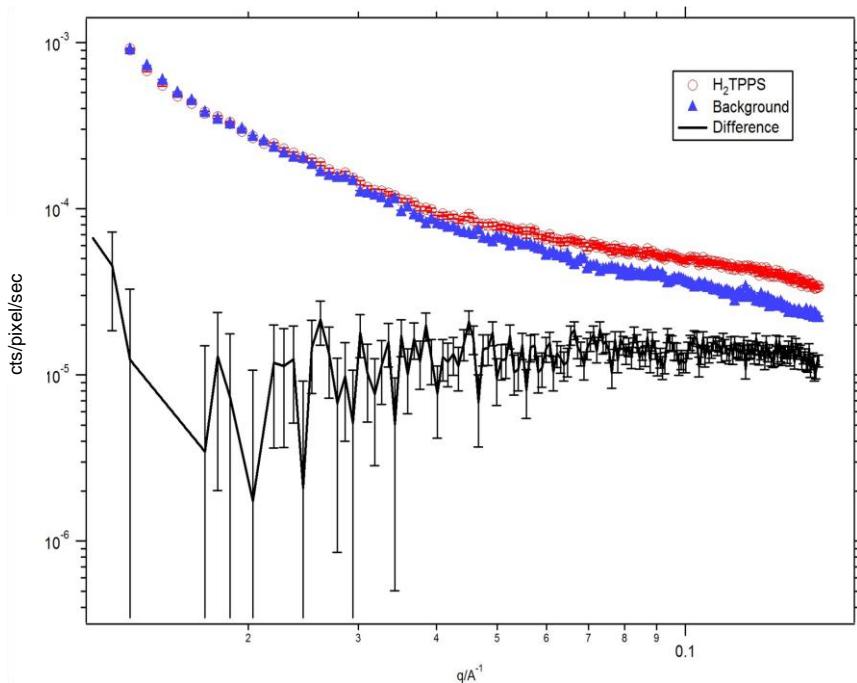

Figure 3.3 Experimental SAXS data from H_2TPPS in aqueous solution at pH 4. The scattering profiles include the sample, background (solvent), and their difference.
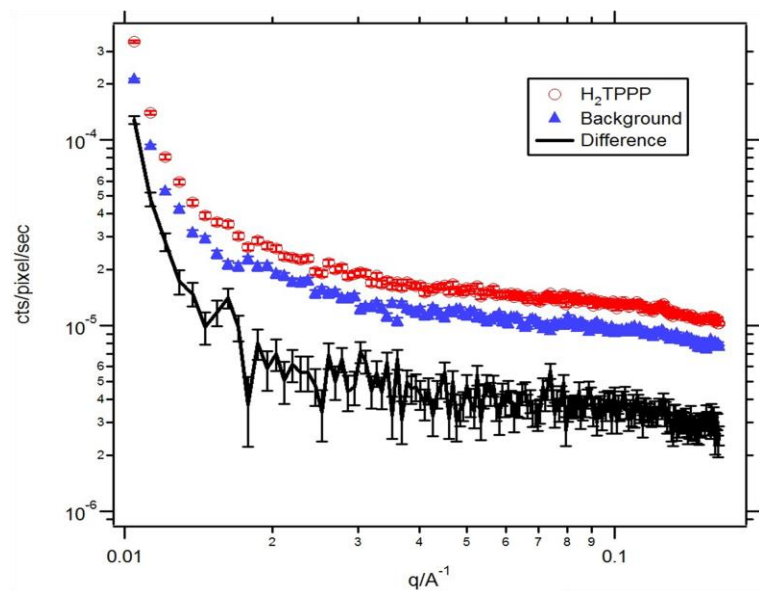

Figure 3.4 Experimental SAXS data from H_2TPPP in aqueous solution at pH 5. The scattering profiles include the sample, background (solvent), and their difference.

Another SAXS experiment was performed on H_2TPPS under improved instrumental conditions. The first pinhole used in the initial scattering experiments was 200 microns in diameter. At this size, the number of counts per second was very low. Though ~10^9 x-rays were being generated by the synchrotron source, only a small amount actually passed through the pinhole opening. The installation of a larger pinhole (400 micron) increased the amount of x-ray flux by a factor of 3. Over 2 million counts were gathered for H_2TPPS within a time span of 2 hrs, which was a drastic increase. However, the expected oscillation peaks were yet to be clearly visible in the $I(q)$ vs q plot (Figure 3.5). Similar to before, the reduced curve was mostly immersed in noise. But this time, in the higher q range, the scattering signal from the sample eventually rises above the background. This observation suggested that perhaps decreasing the Sample-to-detector distance would reveal more information that was hidden in the noise.

Figure 3.5 Experimental SAXS data from H_2TPPS in aqueous solution at pH 4 under improved instrumental conditions. The scattering profiles include the sample, background (solvent), and their difference.

The intensity curves for H_2TPPP and H_2TPPS were further analyzed in Guinier plots (Figure 3.6). From the plots, the radius of gyration (R_g) was calculated based on the slope of the linear region. Due to the weak scattering, the obtained values were not absolutely valid. The calculated slope was very sensitive with respect to the selected regions along the curve. For H_2TPPP, the calculated R_g was 14.78 ± 10.4 Å, which was much smaller than texpected. The calculated R_g for H_2TPPS was 33.08 Å for the steep initial slope and 19.94 ± 12.8 Å for the linear region that followed. It was later concluded that the steeper slope was probably due to residuals from the beamstop, leading to a false calculation. Compared to the calculated R_g value of 70.5 ± 0.5 Å reported in literature,[11] the false value was still too small. The reported[11] size of the porphyrin monomer is ~19 Å. Upon determining the perimeter of the cross-section of the aggregates, the number of porphyrins composing the self-assembled complex can be estimated.
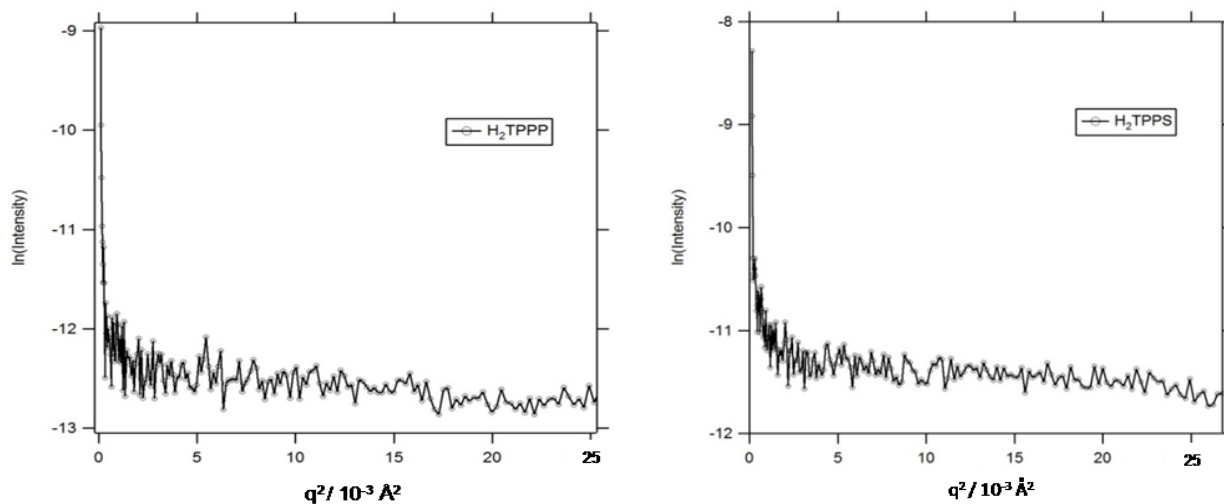

Figure 3.6 Guinier plots of the scattering curves for H_2TPPP (left) and H_2TPPS (right). The slope of the linear regions provides an approximated R_g value.

SAXS studies on self-aggregated H_2TPPS were reported by Dr. Gandini et al.. A proposed structural model was generated based on their experimental scattering data (Figure 3.7). Their models suggest that the J-aggregates form a cylindrical geometry composed of 26 porphyrins, and approximately 3,000 molecules forming H-type aggregates. The obtained

analytical ultracentrifugation data in chapter 2 yielded an average molecular weight of 25,397.9 ± 3,153 g·mol^{-1}, which is in agreement with the 26 porphyrin complex. No such model has been proposed for the self-aggregation of H$_2$TPPP.
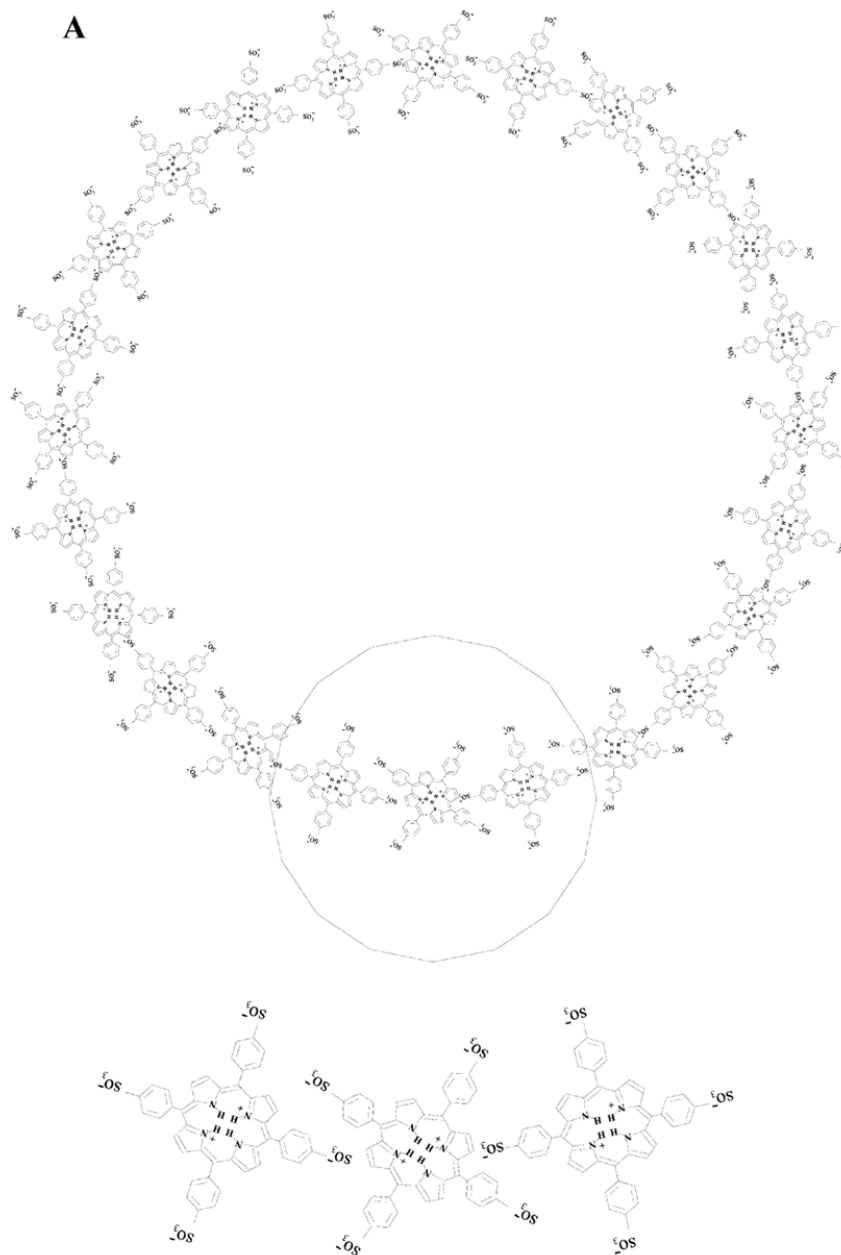
Figure 3.7A Top view model of H$_2$TPPS J-aggregates at pH 4 simulated from SAXS curves.[11]
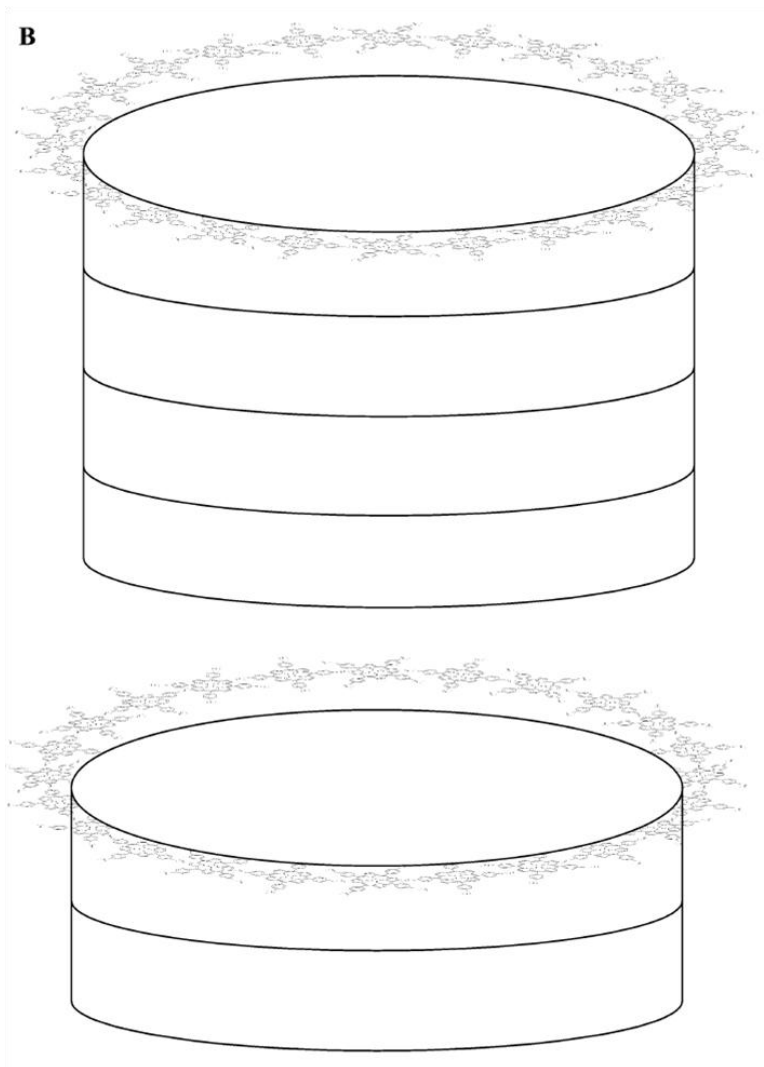
Figure 3.7B Model of H_2TPPS H-aggregates at pH 4 simulated from SAXS curves. Illustrated is an overall view of the hollow cylinder formation.[11]

3.6 Conclusion

Several attempts were made in investigating the structural features of the self-assembled porphyrins. Due to instrumental limitations, the expected scattering data was not attained. However, different methods of optimization were discovered as a result improving the study. SAXS is a very promising application for determining the aggregate morphology in solution. In fact, proposed models of H_2TPPS in solution at pH 4 has been generated based on the scattering

data, but not for H_2TPPP. Once accurate experimental data are achieved, a model will then be proposed to advance the understanding of hierarchical self-assembly.

3.7 Future Work

Further SAXS experiments include decreasing the Sample-to-detector distance to obtain meaningful scattering information from within the noise of the reduced curve. Alternatively, samples will be further examined at a more advanced synchrotron source to overcome the posed challenges of dilute solutions.

3.8 Experimental to Chapter 3

SAXS experiments were performed on a synchrotron beamline at the Louisiana State University Center for Advanced Microstructures and Devices (CAMD), Baton Rouge, Louisiana. Cu Kα radiation generated at 8 KeV was used to analyze the porphyrins samples at room temperature. Silver behenate was the calibration standard. Samples were injected and sealed in 1.0 mm Glaskapillaren capillaries. Data were analyzed using the IGOR Pro software program.

3.9 References

1. Lindner, P.; Zemb, T. *Neutron, X-Ray and Light Scattering: Introduction to an Investigative Tool for Colloidal and Polymeric Systems*. Elsevier Science Publishers B.V.: Bombannes, 1990.

2. Stribeck, N. *X-Ray Scattering of Soft Matter*. Springer Berlin Heidelberg: 2007.

3. King, S. M. Small Angle Neutron Scattering 1995. http://www.isis.rl.ac.uk/ (accessed Jan 2009).

4. Roe, R.-J. *Methods of X-Ray and Neutron Scattering in Polymer Science*. Oxford University Press: New York, 2000.

5. Glatter, O.; Kratky, O. *Small Angle X-Ray Scattering*. Academic Press London: 1982.

6. Shrestha, L. K.; Glatter, O.; Aramaki, K. *J. Phys. Chem. B* **2009**, *113*, 6290-6298.

7. Mariani, P.; Spinozzi, F.; Federiconi, F.; Amenitsch, H.; Spindler, L.; Drevensek-Olenik, I. *J. Phys. Chem. B* **2009**, *113*, 7934-7944.

8. Li, D.; Han, B.; Huo, Q.; Wang, J.; Dong, B. *Macromolecules* **2001,** *34*, 4874-4878.

9. Yuguchi, Y. *Trends in Glycoscience and Glycotechnology* **2009,** *21*, 1-12.

10. Iampietro, D. J.; Brasher, L. L.; Kaler, E. W.; Stradner, A.; Glatter, O. *J. Phys. Chem. B* **1998,** *102*, 3105-3113.

11. Gandini, S. C.; Gelamo, E. L.; Itri, R.; Tabak, M. *Biophys. J.* **2003**, *85,* 1259-1268.

VITA

Javoris Hollingsworth was born in Jeffersonville, Georgia, to Sandra and Garry. He received his Bachelor of Science in Chemistry from Georgia Southern University in May 2007. He is a Gates Millennium Fellow and will be receiving his Master of Science degree from Louisiana State University on August 7, 2009.